

**A NEW APPROACH TO EVALUATE FRACTURE
STRENGTH OF UV-LIGA FABRICATED NICKEL
SPECIMENS**

A Thesis

Submitted to the Graduate Faculty of the
Louisiana State University and
Agricultural and Mechanical College
in partial fulfillment of the
requirements for the degree of
Master of Science in Mechanical Engineering

in

The Department of Mechanical Engineering

by
Catherine Oropeza
B.S., Duke University, 1997
May 2002

To my mother, father, and sister

ACKNOWLEDGMENTS

First and foremost, I thank God for having given me the strength and determination to face the challenges and handle the unpredictable course of this period of my life. Secondly, I am thankful to my family who has always has been the biggest inspiration on a personal and academic level, and has given me unconditional love and support.

Also, I would like to express my appreciation to Dr. Wanjun Wang for giving me the opportunity to take part in this exciting research project and offering me his suggestions, support, and patience throughout the process. I am also grateful to have had Dr. Michael Murphy and Dr. Elizabeth Podlaha as my professors during the earlier stages of my graduate studies and as my committee members.

My sincere gratitude is given to the management and staff at the Center for Advanced Microstructures and Devices (CAMD), especially Dr. Jost Goettert and Dr. Kun Lian, for having provided me with the facilities, equipment, and financial support necessary for this research. Likewise, my appreciation is extended to Dr. Yohanness Desta, Dr. Linke Jian, Tracy Morris, Shaloma Malveaux, Dawit Yemane, and Yoonyoung Jin for all of their great technical and administrative assistance without which this project would never have been possible.

I am also thankful to my research group members, John Williams, Khee-hang Heng, and Ren Yang, as well as my colleagues at the Microsystems (μ set) Lab, John Fuller, Abhinav Bhushan, Summer Dann-Johnson, Dinakar Palaparti, Kevin Zanca, and Proyag Datta, for their invaluable help.

Finally, thanks to all of my friends at LSU who gave me a shoulder to cry on during bad times, and were ready make me smile and have fun with me during the good times.

TABLE OF CONTENTS

ACKNOWLEDGMENTS.....	iii
LIST OF TABLES.....	vii
LIST OF FIGURES.....	viii
ABSTRACT.....	x
CHAPTER 1 INTRODUCTION.....	1
CHAPTER 2 BACKGROUND.....	5
2.1 Definition of Failure Mode and Fracture.....	5
2.2 Fracture Mechanics.....	6
2.2.1 Griffith Crack Theory.....	6
2.2.2 Energy Release Rate Analysis and Fracture Toughness.....	7
2.2.3 Dislocation Theory and Linear Elastic Fracture Mechanics.....	8
2.2.4 Stress Analysis of Cracks.....	10
2.2.5 Plane Stress Versus Plain Strain.....	12
2.2.6 Plasticity Considerations.....	13
2.2.7 Plane-Strain Fracture Toughness Testing.....	14
CHAPTER 3 ELECTROCHEMICAL DEPOSITION.....	16
3.1 Basic Concepts and Mechanism of Electrodeposition.....	16
3.2 The Electrodeposit.....	19
3.2.1 Structure.....	19
3.2.2 Hardness.....	20
3.2.3 Mechanical Properties.....	20
3.2.4 Internal Stress.....	22
3.2.5 Conditions Affecting the Structure and Properties.....	22
3.3 Electrodeposition of Copper.....	25
3.4 Electrodeposition of Nickel.....	25
3.4.1 Electroplating Baths and Their Properties.....	26
3.4.2 Process Quality Control.....	28
3.4.3 Parameters and Procedure.....	30
CHAPTER 4 SPECIMEN DESIGN AND FABRICATION.....	33
4.1 Specimen Configuration and Dimensions.....	33
4.2 Microfabrication.....	38
4.2.1 Microfabrication Issues.....	38
4.2.2 UV Mask Fabrication.....	41
4.2.3 Substrate Cleaning and Preparation.....	43
4.2.4 SU-8 Negative Photoresist.....	44
4.2.5 SU-8 Photoresist Removal.....	46
4.2.6 Copper Sacrificial Layer Etching.....	47

4.2.7 Fabrication Sequence.....	48
CHAPTER 5 TESTING MECHANISM.....	55
5.1 Description of The Testing Mechanism.....	55
5.2 Testing Procedure.....	58
5.3 Testing Related Calculations.....	59
CHAPTER 6 RESULTS.....	63
6.1 UV-LIGA Fabrication Results.....	63
6.1.1 Dimensional Change.....	63
6.1.2 Nickel Specimen Electrodeposition.....	64
6.1.3 Freestanding Nickel Specimens.....	64
6.1.4 SU-8 Removal.....	65
6.2 Preliminary Fracture Testing Results.....	67
6.2.1 Fracture Surface.....	69
CHAPTER 7 SUMMARY AND RECOMMENDATIONS.....	70
REFERENCES.....	73
VITA.....	78

LIST OF TABLES

Table 3-1	Standard Electrode Potentials.....	18
Table 3-2	Strength and Ductility Data for Electrodeposited Metals.....	21
Table 3-3	Nickel Electroplating Solutions.....	27
Table 3-4	Nickel Sulfamate Electroplating Bath Composition.....	30
Table 3-5	Nickel Electroplating Parameters.....	32
Table 4-1	Sacrificial Layer Selection.....	39
Table 4-2	Copper Etchant Selection.....	47
Table 4-3	Processing Parameters for Sacrificial Layer.....	51
Table 4-4	Processing Parameters for Structural Layer.....	52
Table 4-5	Processing Parameters for Final Fabrication Steps.....	53
Table 5-1	Breakdown of Testing Mechanism.....	56
Table 6-1	Relative Dimensional Change.....	63
Table 6-2	Fracture Strength Values for Specimens 9-11.....	69

LIST OF FIGURES

Figure 2-1	Basic modes of crack displacement.....	10
Figure 3-1	Electrodeposition cell.....	17
Figure 3-2	Qualitative effects of operating conditions on the properties of nickel electrodeposited from Watts and sulfamate solutions.....	26
Figure 3-3	Nickel electroplating setup.....	31
Figure 4-1	Specimen layout on sample (wafer).....	34
Figure 4-2	Fracture specimen configuration.....	35
Figure 4-3	Fracture specimen dimensions (μm).....	36
Figure 4-4	Sacrificial layer UV-mask design.....	42
Figure 4-5	Nickel surface before and after copper etching (40X magnification).....	48
Figure 4-6	Schematic of sample fabrication sequence.....	54
Figure 5-1	Fundamental mechanical elements of the testing setup.....	57
Figure 5-2	Testing mechanism information flow diagram.....	58
Figure 6-1	Single UV-LIGA fabricated specimen on alumina substrate.....	65
Figure 6-2	Measurescope image of single freestanding notch and guiding blocks revealing specimen sidewalls.....	65
Figure 6-3	Partial Scanning Electron Microscope (SEM) image of tensile specimen enhancing the gap between the bottom of the nickel structure and the ceramic wafer.....	66
Figure 6-4	SEM image of perforation at pinning end of fracture specimen containing SU-8 residue.....	67
Figure 6-5	Partial SEM image of fracture specimen showing SU-8 remains on one side of the stem.....	67
Figure 6-6	Force as a function of displacement with fracture force values represented for specimens 10-12 and trendline revealed by specimen 9.....	68

Figure 6-7 Stitched SEM image of the fracture surface of specimen 11..... 69

ABSTRACT

One of the major difficulties faced by MEMS researchers today is the lack of data regarding properties of electroplated metals or alloys at micro-levels as those produced by the LIGA and LIGA related process. These mechanical properties are not well known and they cannot be extrapolated from macro-scale data without experimental verification. This lack of technical information about microscale physical properties has affected the consistency and reliability of batch-fabricated components and leads to very low rates of successful fabrication. Therefore, this material issue is of vital importance to the development of LIGA technology and to its industrial applications.

This thesis focuses on the development of a new capability based on design, fabrication, and testing of groups of UV-LIGA fabricated nickel microspecimens for the evaluation of fracture strength.

The design of the test specimens involved determining the appropriate dimensions and configuration based on a set of criteria dictated by the objectives of the project. Likewise, the development of the specimens required some experimentation with different microfabrication techniques, and combinations thereof, to generate a final fabrication sequence that would produce suitable freestanding, wafer-bound specimens.

The devised testing mechanism demonstrated compatibility with the fabricated samples and capability of performing the desired experimentation by generating resistance-to-fracture values of the nickel specimens. The average fracture strength value obtained, expressed with a 95% confidence interval, was 315 ± 54 MPa.

Preliminary testing results proved that further data acquisition, especially involving tensile specimen testing, and material analysis is needed to fully understand the implications of the information obtained. The products of this new microspecimen testing approach can be extended for use with other microfabricated metals and metal alloys, particularly on a more qualitative, comparative basis.

CHAPTER 1 INTRODUCTION

The most evident tendency of the technological advances of the last century is miniaturization. The ever-decreasing size of hi-tech devices has become a symbol/trademark for faster and better performance. Although the latter does not necessarily hold true for all cases, there are a number of instances where the potential for added functionality within a fraction of the area along with faster response time, greater sensitivity/precision, and less power consumption has opened up a new realm of possibilities for the development of microscale mechanical, electrical, magnetic, optical, pharmaceutical, biomedical, and fluidic devices. This new approach has spawned a number of fast-growing technologies in the 21st century, one of which is Microelectromechanical Systems (MEMS).

MEMS is the integration of mechanical and/or optical elements, sensors, actuators, and electronics on a common silicon substrate through the utilization of microfabrication technology. While the electronics are fabricated using integrated circuit (IC) process sequences (e.g., CMOS, Bipolar, or BICMOS processes), the micromechanical components are fabricated using compatible micromachining processes that selectively etch away parts of the silicon wafer or add new structural layers to form devices with dimensions ranging from subcentimeters to submicrometers.

MEMS promises to revolutionize nearly every product category by bringing together silicon-based microelectronics with micromachining technology, thereby, making possible the realization of complete systems-on-a-chip. This new manufacturing technology has several distinct advantages. First, MEMS is an extremely diverse technology that potentially could significantly impact every category of commercial and

military products. Already, MEMS is used for everything ranging from in-dwelling blood pressure monitoring to active suspension systems for automobiles. The nature of MEMS technology and its diversity of useful applications make it a potentially far more pervasive technology than even integrated circuit microchips.

Both micromachining and microelectronics fabrication start with lithography, the technique used to transfer copies of a master pattern onto the surface of a solid material [1]. The origins of this method date back to 1822 when Frenchman Nicéphore Niépce copied an etched print on oiled paper by placing it over a glass plate covered with bitumen dissolved in lavender oil. In 1975, Romankiw and coworkers at IBM pioneered a process to create high aspect ratio metal structures by electroplating gold into resist patterns defined by means of X-ray lithography. Ehrfeld et al. (Kernforschungszentrum Karlsruhe, Germany, 1982) added a final molding step to Romankiw's process and created what is known today as the LIGA technique. LIGA is the German acronym for lithography (lithographie), electrodeposition (galvanoförmung), and molding (abformtechnik) [1]; it is a promising new micromachining technology capable of batch fabrication of microelectromechanical components at a relatively low cost.

Most current MEMS devices use polycrystalline silicon (polysilicon) produced by chemical vapor deposition (CVD) processing as their structural material. While polysilicon has a high strength-to-weight ratio which allows for very high bandwidth mechanical devices to be realized, and thus makes it an attractive choice for many high-performance mechanical applications (accelerometers, pressure transducers, etc.), the nature of the manufacturing process places severe limitations on the thickness of the

resulting film (few micrometers) and consequently the fabricated components. As a result, polysilicon is not a suitable choice of material for a wider-range of applications imposing large sustained forces and torque loadings on the microfabricated elements. LIGA offers significant advantages in this direction yielding structures that can easily be manufactured on the order of hundreds of micrometers in thickness with a high precision, giving them great versatility and potential in MEMS applications.

The structural materials of LIGA fabricated devices are metals and metal alloys produced by electrochemical deposition into resist patterns generated by X-ray lithography. The mechanical properties of electrodeposited materials are, in general, different from those of bulk materials. In fact, the mechanical properties of these thick films are not well known and they cannot be extrapolated from macro-scale data without experimental verification. Thus, one of the major difficulties faced by researchers today is the lack of data regarding properties of electroplated metals or alloys at micro-levels as those produced by the LIGA process. This lack of technical information about microscale physical properties has affected the consistency and reliability of batch-fabricated components and leads to very low rates of successful fabrication. Therefore, this material issue is of vital importance to the development of LIGA technology and to its industrial applications.

So far, most of the previous and current efforts in the area of MEMS materials testing and characterization have concentrated on determining mechanical behavior of polysilicon [2-16]. To date there have been few initial attempts at testing LIGA produced microcomponents. These previous efforts were only concerned with tensile or bending of beam specimens and have resulted in values for the yield strength, ultimate

tensile strength, and Young's modulus, mainly of LIGA nickel [17-26]. However, there is very little agreement among these studies, more than likely due to problems arising from specimen handling, inadequate testing capabilities and/or differences in electroplating conditions used during fabrication.

This thesis focuses on the development of a new capability based on design, fabrication, and testing of groups of Ultra Violet-LIGA (UV-LIGA) fabricated microspecimens for the evaluation of fracture strength. In particular, the following effort reveals: (a) the design and successful fabrication methods of suitable free-standing, wafer-bound specimens, (b) a corroboration/validation of the compatibility of the samples and the devised testing mechanism, and (c) resistance-to-fracture values of UV-LIGA nickel produced by this testing mechanism. Chapter 2 will present a general understanding of fracture toughness and some of its testing related considerations; the following chapter describes the underlying principles of electrochemical deposition and the structure and properties of the electrodeposits. Following will be a discussion of specimen dimensional characteristics and fabrication procedures. Lastly, Chapter 5 will present an overview of the testing mechanism and Chapter 6 will describe the fabrication and preliminary test results.

CHAPTER 2 BACKGROUND

2.1 Definition of Failure Mode and Fracture

Collins (1993) defined mechanical failure as any change in the size, shape, or material properties of a structure, machine, or machine part that renders it incapable of satisfactorily performing its intended function. Therefore, failure mode is the process or processes whose individual or combined effects produce failure [27].

A reasonable approach to the classification of all possible failure modes is based on the definition of three main categories: manifestations of failure (elastic deformation, plastic deformation, rupture or fracture, and material change), failure-inducing agents (force, time, temperature, and reactive environment), and locations of failure (body type and surface type). In this way, every distinct failure mode can be defined as a combination of one or more manifestations of failure with one or more failure inducing agents, and a failure location. Literally hundreds of combinations can be systematically listed.

One of the failure modes most commonly observed in practice involves the rupture or fracture of a mechanical part. Specifically, ductile rupture occurs when the plastic deformation, in a part that exhibits ductile behavior, is carried to the extreme so that the member separates into two pieces. Initiation and coalescence of internal voids slowly propagate to failure, leaving a dull, fibrous rupture surface. On the other hand, brittle fracture occurs when the elastic deformation, in a part exhibiting brittle behavior, is carried to the extreme so that the primary interatomic bonds are broken and the member separates into two or more pieces. Preexisting flaws or growing cracks are

initiation sites for very rapid crack propagation to catastrophic failure, leaving a granular, multifaceted fracture surface [27].

2.2 Fracture Mechanics

As suggested earlier, the fracture behavior of a given material will depend on factors such as the stress level, presence of a flaw, material properties, and the mechanism(s) by which the fracture proceeds to completion. The purpose of the following subsections is to establish quantitative relationships between a few of these factors and describe some of the basic concepts involved in the important tool of engineering analysis called fracture mechanics.

2.2.1 Griffith Crack Theory

The first approach to analyze the strength and deformation of engineering metals explored the solid state physics of material behavior through a simple atomic model of metallic elements. However, it was noted that the estimation of the shearing strength of crystalline metals by theoretical consideration of atomic bonding forces lead to strength estimates of several million pounds per square inch whereas observed yield strengths values ranged one or two, sometimes even five, orders of magnitude less. Also, experimentally determined elastic deformations were much greater for a given load than would be predicted on a theoretical basis. Crystals exhibited greater strength after deformation than before, and mechanical properties varied with changes in temperature.

The discrepancy between the theoretical strengths and the actual strengths of these materials implied the existence of cracks or defects within the structure of the metals, which concentrate the stress to an extent that the theoretical failure strength is locally exceeded to initiate failure. In 1920 A. A. Griffith postulated that brittle

materials contain many submicroscopic cracks that are caused to grow to a macroscopic size upon the application of a sufficiently high stress, finally causing brittle fracture [27].

Griffith's theory was modified by Orowan to account for the degree of plasticity always present in the brittle fracture of metals, according to which the fracture stress is given by:

$$\mathbf{s}_f \approx \left(\frac{E\gamma_p}{a} \right)^{1/2} \quad (2.1)$$

where E is Young's modulus and γ_p is the plastic work required to extend the crack wall of a crack of length $2a$.

2.2.2 Energy Release Rate Analysis and Fracture Toughness

Equation (2.1) was modified by Irwin to replace γ_p , which is hard to quantify experimentally, with a term that is directly measurable [28].

$$\mathbf{s}_f = \left(\frac{EG_c}{\mathbf{p}u} \right)^{1/2} \quad (2.2)$$

where G_c represents the critical value of the crack-extension force.

G may also be considered the rate of transfer of energy from the elastic stress field of the cracked structure to the inelastic process of crack extension, i.e., the strain-energy release rate.

$$G = \frac{\mathbf{p}u\mathbf{s}^2}{E} \quad (2.3)$$

The critical value of G that causes the crack to propagate to fracture, G_c , is called the fracture toughness of the material and it is determined from the load, P_{\max} , at which the crack runs unstable to fracture.

$$G_c = \frac{P_{\max}^2}{2} \frac{\partial(1/M)}{\partial a} \quad (2.4)$$

In Equation (2.4), $1/M$ represents the compliance of the cracked plate, which depends on the crack size. Once the compliance versus crack-length relation has been established for a given specimen geometry, G_c can be obtained by simply noting the load at fracture, provided the amount of plastic deformation at the tip is kept to a minimum [29].

Fracture toughness is probably one of the most important mechanical properties from a manufacturing standpoint because it expresses the material's resistance to fracture. Any micro-component with low fracture toughness, or equivalently very brittle, can suffer from catastrophic failure leading to device malfunction and finally failure. In view of the small dimensions (small volumes) involved in MEMS components and due to the fact that a material's fracture toughness is very sensitive to flaws or defects present, it is evident that the evaluation of this property can lead to optimization of LIGA processing conditions.

2.2.3 Dislocation Theory and Linear Elastic Fracture Mechanics

The developments of Griffith, Orowan, and Irwin improved the agreement between theoretical estimates and experimental values of strength of engineering metals and contributed to the understanding of the behavior of these materials under applied loads. In fact, these efforts laid the foundation for the development of the two most

important tools in terms of the strength and deformation of engineering metals, namely, dislocation theory and linear elastic fracture mechanics.

Dislocation theory was the first postulation to fully explain the discrepancies between theoretical calculations and experimental measurements without making any questionable assumptions. The scientific basis implies the existence of imperfections within the crystal structure that can be moved by the application of low stress levels to cause plastic deformation. These lattice imperfections are called dislocations, and the concept of mobility of a dislocation was the missing ingredient that made this theory so superior to all preceding bodies of work. Following the notion of mobile dislocations, intensive investigation corroborated the presence of dislocations in all engineering metals.

The emergence of dislocation theory has made great progress in explaining the mechanisms of deformation and fracture of engineering metals at the atomic level, however, it does not supply engineers with the quantitative tools necessary to estimate potentially critical combinations of loading, geometry, and material properties. Therefore, motivated by the large number of ship and machine failures which took place in the 1940's to 1960's, a group of engineering researchers worked at the macroscopic level to develop predictive models in engineering structures and machines. Consequently, it was recognized that the most successful approach to prediction and prevention of fracture is to model the behavior at the crack tip as simple as possible, yet include all significant measurable or calculable variables such as crack length, state of stress and fracture toughness. The simplest, most useful model, so far, for stress at a

crack tip is based on the assumptions of linear elastic material behavior and a two-dimensional analysis; thus it is referred to as linear elastic fracture mechanics.

2.2.4 Stress Analysis of Cracks

There are three basic types of stress field defined for crack-tip stress analysis, each one is associated with a distinct mode of loading depicted below.

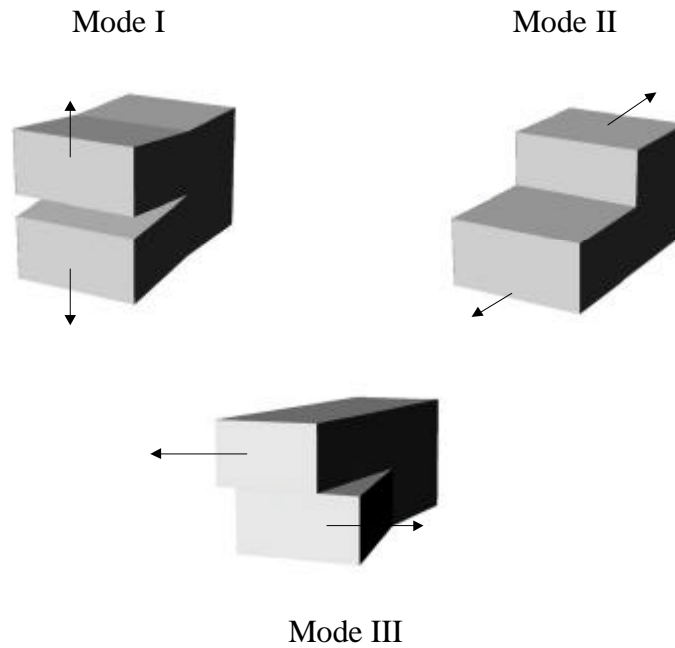


Figure 2-1 Basic modes of crack displacement

Mode I is an opening or tensile mode, where the crack walls move directly apart. Mode II is a sliding or in-plane shearing mode, where the crack walls slide over one another in a direction perpendicular to the leading edge of the crack. Finally, mode III is a tearing or antiplane shearing mode, where the crack walls slide away from each other in a direction parallel to the leading edge of the crack [29]. Mode I is by far the most frequently encountered mode of crack deformation in common engineering practice. As a result, a considerable amount of effort has been directed to developing analytical and

experimental methods to quantify the stress-crack relationships under this type of loading.

Irwin pointed out that the local stresses near a crack depend on the product of the nominal stress, \mathbf{s} , and the square root of the half-flaw length. He called this relationship the stress intensity factor, K , where for a sharp elastic crack in an infinitely wide plate, K is defined as:

$$K = \mathbf{s}(\rho l)^{1/2} \quad (2.5)$$

The stress intensity factor is a convenient way of describing the stress distribution around a flaw. If two flaws of different geometry have the same value of K , then the stress fields around each of the flaws are identical. Values of K for many geometrical cracks and many types of loading can be calculated using the theory of elasticity. For the general case the stress intensity factor is given by:

$$K = \mathbf{a}\mathbf{s}(\rho l)^{1/2} \quad (2.6)$$

where \mathbf{a} is a parameter that depends on the specimen and crack geometry. For example, for a plate of width w loaded in tension with a centrally located crack of length $2a$ the stress intensity factor is defined by Equation (2.7) below [28].

$$K = \mathbf{s}(\rho l)^{1/2} \left(\frac{w}{\rho l} \tan \frac{\rho l}{w} \right)^{1/2} \quad (2.7)$$

There are two extreme cases for mode I loading. With thin plate-type specimens the stress state is plane stress, while with thick specimens there is a plain-strain condition. The plain-strain condition represents the more severe stress state and the values of K_c are lower than for plane-stress specimens.

By combining Equation(2.3) and Equation (2.5) it is evident that G and K are simply related, thus establishing a relationship between the energy rate and stress field approaches.

$$K^2 = GE \quad (2.8)$$

$$K^2 = \frac{GE}{(1-n^2)} \quad (2.9)$$

where Equation (2.8) refers to the plane-stress case and Equation (2.9) refers to the plane-strain case.

2.2.5 Plane Stress Versus Plain Strain

The plastic-zone size depends on the state of stress acting at the crack tip. When the sample is thick in a direction parallel to the crack front, a large induced tensile stress can be generated that will restrict plastic deformation in that direction. Since the fracture toughness of a material will depend on the volume of material capable of plastically deforming prior to fracture, which in turn depends on the specimen thickness, then the value of K_c will vary with thickness. As such, with a thin sample, where the degrees of plastic constraint at the crack tip are minimal, the plane-stress condition will dominate and the material will exhibit maximum toughness (note that if the specimen thickness is further reduced from this lower limit, the toughness value falls due to the fact that the amount of material available to absorb the plastic deformation energy also decreases). Conversely, if the sample is thick, and a condition of crack-tip plastic-constraint and thus plain-strain exists, the toughness of the material will reduce dramatically. Likewise, the lower level of toughness also reaches a plateau after which point increasing the thickness does not change its value. Consequently this

measure, designated as plain-strain fracture toughness, K_{Ic} , is considered a conservative lower limit of material toughness in any given engineering application.

To summarize, plane-stress fracture toughness is related to both metallurgical characteristics and specimen geometry whereas plain-strain fracture toughness depends only on metallurgical factors. Hence, a comparison of the inherent toughness levels of materials of different thickness should be based on K_{Ic} values.

2.2.6 Plasticity Considerations

As previously described, a region of plasticity arises near the crack tip whenever the distribution of stresses in this vicinity exceeds the yield strength, \mathbf{s}_{ys} , of the material. In order to estimate the size of this zone it is necessary to consider the stresses just ahead of the crack tip. At some distance $r = r_p$ from the crack tip the elastic stress, \mathbf{s}_y , will exceed the yield strength, thereby truncating the elastic stress at that value. Thus, r_p is the size of the plastic zone and it can be computed as shown below.

$$\mathbf{s}_y = \frac{K}{(2r_p)^{1/2}} = \mathbf{s}_{ys} \quad (2.10)$$

$$r_p = \frac{K^2}{2p\mathbf{s}_{ys}^2} = \frac{\mathbf{s}_y^2 a}{2\mathbf{s}_{ys}^2} \quad (2.11)$$

Irwin proposed that the existence of a plastic zone makes the crack act as if it were longer than its physical size. In other words, as a result of crack-tip plasticity the displacements are larger and the stiffness is lower than for the strictly elastic situation. The usual correction is to assume that the effective crack length is the actual length plus the radius of the plastic zone [28].

$$a' = a_{eff} = a + r_p \quad (2.12)$$

where

$$r_p \approx \frac{1}{2} \frac{K^2}{\sigma_{ys}^2} \quad (2.13)$$

$$r_p \approx \frac{1}{6} \frac{K^2}{\sigma_{ys}^2} \quad (2.14)$$

Equations (2.13) and (2.14) refer to the plane-stress and plain-strain cases, respectively. The smaller value of r_p in plane strain is consistent with the fact that the triaxial stress field limits the amount of plastic deformation.

2.2.7 Plane-Strain Fracture Toughness Testing

The criterion for brittle fracture in the presence of a crack-like defect is rapid and unstable crack propagation carried to failure when the stresses at the crack tip exceed a critical value. Since the stresses at the crack tip can be described by the stress intensity factor, K , then a critical value of this parameter is used to define the conditions for brittle failure. Given that the usual test involves mode I-type loading, the aforementioned critical value is designated as K_{Ic} .

The American Society for Testing and Materials (ASTM) has designed a methodology to obtain fracture toughness values of brittle materials in the laboratory, described in Standard E399-90. According to this procedure, a recommended test sample is initially fatigue-loaded, in a low-cycle high-strain mode, to extend the machined notch a prescribed amount. (The three most common sample configurations denoted in the fracture toughness ASTM Standard are: the compact tension specimen, the three-point bend specimen, and the notched round specimen; each of which is very carefully specified within). Subsequently, a continuous log of load versus relative displacement at the open end of the notch (proportional to crack displacement) is taken

until the onset of fracture. The maximum load at fracture is recorded and its value is used to calculate the fracture toughness of the material [30].

Brown and Strawley determined empirically that the minimum value of both thickness and crack length to achieve plain-strain conditions and valid K_{Ic} measurements is [29]:

$$t, a \geq 2.5 \left(\frac{K_{Ic}}{s_{ys}} \right)^2 \quad (2.15)$$

CHAPTER 3 ELECTROCHEMICAL DEPOSITION

3.1 Basic Concepts and Mechanism of Electrodeposition

Mohler (1969) defined the electrodeposition process as one in which electric current is carried across an electrolyte and a substance is deposited at one of the electrodes [31]. The electrolyte is a solution that carries the current by means of ions. The ability of a solvent (generally water) to ionize the substances dissolved in it makes the electrolysis possible. The positively charged ions are attracted to the negative electrode or cathode, while the negatively charged ions travel towards the positive electrode or anode. Each electrode reaction takes place at a certain voltage and the most positively charged ions are deposited at the cathode.

When a metal is immersed in an aqueous solution containing ions of that metal M^{z+} there is an exchange of these ions between the two phases, the solid metal and the solution. Some ions from the crystal lattice will enter the solution and some ions from the solution will enter the crystal lattice. After a certain period of time a dynamic equilibrium is reached between the metal, M , and its ions, as denoted below [32]:



where z is the number of electrons involved in the reaction. When the reaction happens from left to right it consumes electrons and is considered a reduction reaction, if the reaction in the opposite direction takes place it releases electrons hence being regarded as an oxidation reaction.

An electrochemical cell consists of at least two electrodes where reactions occur, an electrolyte for conduction of ions, and an external conductor to provide continuity for the circuit [33]. For the specific case of electrodeposition of metals, an external

power supply is included in the system to provide the electrons in the reduction of these metals, as seen in Figure 3-1 (notation is based on Equation (3.1)). The cathode is generally where the metal growth takes place on a given substrate, and the anode undergoes dissolution.

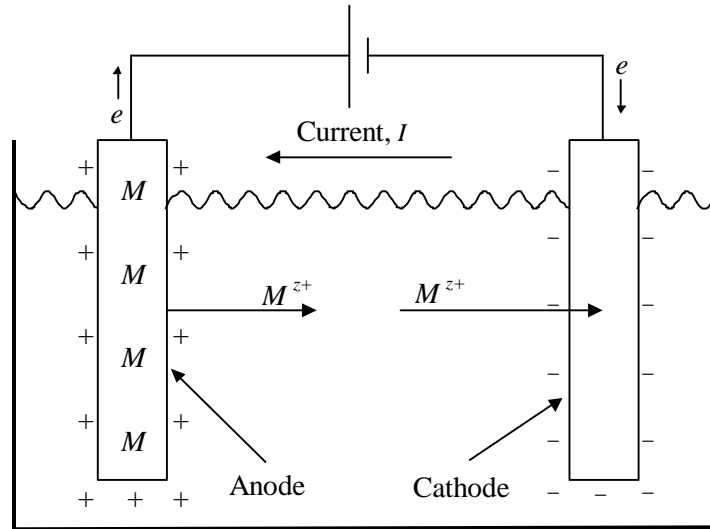


Figure 3-1 Electrodeposition cell

In an electrochemical cell, the result of the charging of the interphase between the metal and the electrolyte solution is the potential difference between these two phases. Any potential measurement of a single electrode must include a second electrode in order to complete the electrical circuit; hence electrode potentials are always measured with respect to another electrode. The electrode designated as the universal standard is the hydrogen electrode. Accordingly, the zero of potential is defined at 25°C and unit activity for hydrogen ions. By connecting another electrode to this half-cell it is possible to measure the potential of this electrode with respect to the hydrogen standard. Table 3-1 contains a list of the values of these potentials for selected

metals [32]. These relative standard electrode potentials are a function of the activity of the metals ions in the solution, that is, they are considered a measure of the oxidizing power of the solution. The potentials reflect the ability of the metal to become ionized.

Table 3-1 Standard Electrode Potentials

Metal/Metal-Ion Couple	Electrode Reaction	Standard Potential Value (V)
Au/Au ⁺	Au ⁺ + e ⇌ Au	1.692
Au/Au ³⁺	Au ³⁺ + 3e ⇌ Au	1.498
Cu/Cu ⁺	Cu ⁺ + e ⇌ Cu	0.521
Cu/Cu ²⁺	Cu ²⁺ + 2e ⇌ Cu	0.3419
Fe/Fe ³⁺	Fe ³⁺ + 3e ⇌ Fe	-0.037
Ni/Ni ²⁺	Ni ²⁺ + 2e ⇌ Ni	-0.257
Zn/Zn ²⁺	Zn ²⁺ + 2e ⇌ Zn	-0.7618

The metal ions displaying a positive voltage are more reactive than the hydrogen ion when they are present in equivalent quantities, while the metal ions having a negative voltage are less reactive than the hydrogen ion. Thus, as the scale is traversed upward, the metal ions become more electropositive (attracted to the cathode), or they deposit more readily. Proceeding in the opposite direction to more negative electrode potentials, the metals become more electronegative, meaning they easily go into solution; these are termed anodic metals.

In the 1830's Michael Faraday predicted a relationship between the charge passed and the amount of a substance oxidized or reduced at an electrode. His proposal was based on two main arguments related to electrolytic processes:

- (a) The amount of product formed is directly proportional to the charge passed.
- (b) For a specified quantity of charge passed, the masses of products formed are proportional to the electrochemical equivalent weights of the products [33].

These principles are embodied mathematically as follows:

$$m = \frac{sMt}{nF} \quad (3.2)$$

Where m is the mass of the substance, s is the stoichiometric coefficient of the species, M is the atomic or molecular weight, I is the current, F is Faraday's constant, n is the number of electrons participating in the reaction, and t is the time elapsed.

3.2 The Electrodeposit

This section will comprise some of the most relevant material science issues related to electroplated films and how these compare to their bulk-produced counterparts.

3.2.1 Structure

Most electrodeposits exist in one of three crystal habitats. The most common one is the face-centered cubic (fcc), followed by the body-centered cubic (bcc). Materials less often display a hexagonal structure [32].

In many films there is a crystal direction that grows faster toward the anode than the other ones. The grains that possess this particular direction can also grow sideways and cover grains of an unfavorable crystal direction. Like so, the film will consist mostly of grains exhibiting the preferred growth direction.

If the grains are not randomly oriented, the condition is called a texture. In the case of electroplated metals the texture is a fiber axis, because, similarly to wire drawn through a die, the directions perpendicular to the preferred orientation are randomly oriented [32].

The crystal form of the deposit is generally in the crystal system normal for the particular metal. However, occasionally the basis metal can influence the structure of

the film to such an extent that the crystal form produced is unusual for that metal. For example, cobalt and chromium have been shown to be electrodeposited in forms not produced by metallurgical means [31].

3.2.2 Hardness

For the case of electrodeposits the qualitative relationships commonly observed in bulk materials between hardness and other properties, such as tensile strength and ductility, do not necessarily hold true. For example, it would be expected that the hardness increases with the tensile strength and decreases with the ductility. However, the reverse effect is common among electrodeposits [32]. Therefore, when dealing with electroplated films, it is important to be able to discern the significance of these types or measurements.

The hardness of a deposit can be influenced by changes in current density or temperature of the electrolyte. Hardness values are also greatly affected by the presence of impurities, organic substances, and addition agents. For some electroplated metals, such as palladium, platinum, iron, and nickel, it is possible to obtain hardness values much greater than those obtained in work hardening [31].

3.2.3 Mechanical Properties

The information currently available in terms of mechanical properties of electroplated films focuses on tensile strength, yield strength, ductility, and modulus of elasticity. Values of tensile strength and elongation percent for a few commonly electrodeposited metals and their wrought counterparts are tabulated below [34].

Table 3-2 Strength and Ductility Data for Electrodeposited Metals

Wrought Metal					
Metal	Min. Tensile Strength (ksi)	Max. Tensile Strength (ksi)	Elongation Percent	Tensile Strength (ksi)	Elongation Percent
Copper	25	93	3 to 35	50	45
Gold	18	30	22 to 45	19	45
Nickel	50	152	5 to 35	46	30
Zinc	7	16	1 to 51	13	32

The moduli of elasticity of electrodeposits are generally smaller than those of metals formed by other means [32]. The conditions under which metals are produced by electrodeposition are different from conventional casting methods. However, the resulting deposit is governed by the laws pertinent to the particular metal. The difficulty in obtaining accurate values and the possibility that the deposits do not behave elastically are both potential reasons for this discrepancy.

The fundamental sources of strength derive from hindrance to dislocation movement. The main dislocations present in electrodeposits are grain boundaries. Thus, additives increase the strength of deposits mostly by refining the grains. On the other hand, codeposited materials can increase the density of dislocations, which, in turn, will prevent the movement of others, and also result in increased strength.

Fine-grained deposits are usually brittle in nature. But, there are instances where the ductility of deposits can actually be larger than it appears to be. Such is the case when necking occurs prior to fracture. The necking phenomenon is limited to a very small volume so the overall plastic deformation is nonetheless small and hence

indicative of poor ductility. However, the ductility, as indicated by the reduction in the cross-sectional area prior to fracture, may be quite good.

3.2.4 Internal Stress

Almost all electrodeposited coatings exist in a state of stress. This stress is frequently referred to as internal because no external forces are applied. The term residual is also used in connection with stress and regularly synonymously with internal [35].

Stresses can be classified as macrostresses or microstresses according to the dimensional scale of the affected region. Macrostresses have the same sign (tensile or compressive) over large areas of the deposits. On the other hand, microstresses, change sign within very small areas so that the net stress is zero over the surface of the deposit. Electroplating technology is mostly concerned with macrostresses, as they can result in dimensional distortions and can affect the fatigue properties, the corrosion resistance and adhesion to substrate. Microstresses manifest themselves primarily as an increase in hardness.

3.2.5 Conditions Affecting the Structure and Properties

The characteristics of electrodeposited metals or metal alloys are mainly influenced by the environment in the immediate vicinity of the cathode. Electrodeposits are undoubtedly crystalline in nature, and the form of the deposit depends largely on two factors: first, the rate of formation of the crystal nuclei by the discharge of the ions at the cathode, and, second, the rate at which these nuclei grow into large crystals. If the conditions are such as to favor the rapid formation of fresh nuclei on the cathode, the deposit will tend to consist of small, fine-grained crystals. The metal being deposited

will then be smooth and relatively hard. On the other hand, if the circumstances are such that the nuclei increase in size rapidly, the deposit will consist of relatively large crystals and will be rough in appearance [36].

There are many parameters that influence the aforementioned factors, namely formation of crystal nuclei and their increase in size, but only the major five contributors will be considered in this text.

- (a) Current Density: At low current densities the discharge of ions happens at a slow rate, allowing for ample crystal-nuclei growth time, consequently the formation of fresh nuclei is unnecessary. The deposits obtained under these conditions exhibit a coarse crystalline structure. As the current density increases, the rate of discharge of the ions also increases, and fresh nuclei will tend to form. Like so, the resulting deposit will consist of smaller crystals. In summary, the increase in current, within certain limits, yields deposits that are more fine-grained. However, there is a definite limit to this improvement, because at very high current densities the crystals tend to grow out from the cathode towards regions where the solution is more concentrated hence creating trees or nodules in the film.
- (b) Concentration of Electrolyte: Increasing the concentration of the solution can largely offset the bad effects caused by electroplating at high current densities. Likewise the use of agitation in the electrolyte will also postpone until much higher current densities these harmful consequences, such as nodule formation.

- (c) Temperature: Increasing the temperature seems to have two effects which counter one another. First of all, it promotes the diffusion of ions to the cathode, thereby preventing impoverishment, which leads to roughness of the deposit. On the other hand, it also increases the rate of growth of the crystal nuclei, so the deposit will have a tendency to be coarse. When operating at moderate temperatures, such as those generally applied to electroplate nickel, the first of the abovementioned effects predominates, thus the deposits are improved. However, at higher temperatures, the quality of the deposit deteriorates.
- (d) Impurities: Electroplated films normally contain various types of inclusions or impurities. The source of these impurities may be from one or more of the following: added chemicals (brighteners, levelers, etc.), added particles (for composite films), cathodic products (complex metal ions), hydroxides (of the depositing metals), and bubbles (hydrogen gas, etc.) [32]. While the effect of a particular additive is frequently specific for a given metal, a general statement can be made relating the purpose of additives and the formation of fine-grained coatings. The addition agents are generally substances that have a high surface activity, i.e. they tend to be adhered to or be absorbed by the surface. Therefore, if the substance covers the crystal nucleus, the further growth of the nucleus will be prevented. The subsequently discharged ions are then forced to create fresh nuclei, which results in a fine-grained deposit. Because the addition agent appends to the crystal nuclei, the films obtained in the presence of additives contain some

proportion of the latter. An excessive amount of additive in the electrolyte can cause the deposit to become brittle and break apart at the crystal interface, where there is a relatively thick layer of the added substance.

- (e) pH: The pH of the solution influences the discharge of hydrogen ions, thus causing the solution in the cathode layer to become alkaline and precipitate hydroxides or basic salts. The inclusion of a significant amount of these compounds will make the resulting deposit exhibit a fine grain structure, but it will be dark in color (burnt), or spongy/powdery in character. Additionally, the evolution of hydrogen gas is often accompanied by the formation of spots and streaks in the film [36].

3.3 Electrodeposition of Copper

Electrochemically deposited copper was employed as a sacrificial layer in the specimen fabrication process. Thus, the deposition technique was aimed to benefit the uniformity and adhesion of the coating to the substrate rather than focusing on the specific structure and properties of the copper deposit.

Copper was electrodeposited at a current density of $15\text{mA}/\text{cm}^2$ for 9 hours at room temperature to obtain a sacrificial layer height of $90\mu\text{m}$. The electroplating was carried out in the cleanroom of the Center for Advanced Microstructures and Devices (CAMD) in Baton Rouge, Louisiana, as described by Heng (2001) [37].

3.4 Electrodeposition of Nickel

The next subsections will outline the major aspects of the nickel deposition process. One of the determining factors in the characteristics of the nickel deposit is the electrolyte composition, thus, a brief discussion about the two main nickel

electroplating baths and their relevant properties will be presented first. Following will be a summary of the aspects involved in the quality control of nickel films. Lastly, the details of the nickel electroplating practice utilized in this study will be given.

3.4.1 Electroplating Baths and Their Properties

Today the Watts nickel electrodeposition solution and the nickel sulfamate solutions are the most widely used for functional plating and for electroforming. The properties of Watts and sulfamate electrolytes can vary in different ways with changing electrodeposition parameters as illustrated qualitatively in Figure 3-2 [32].

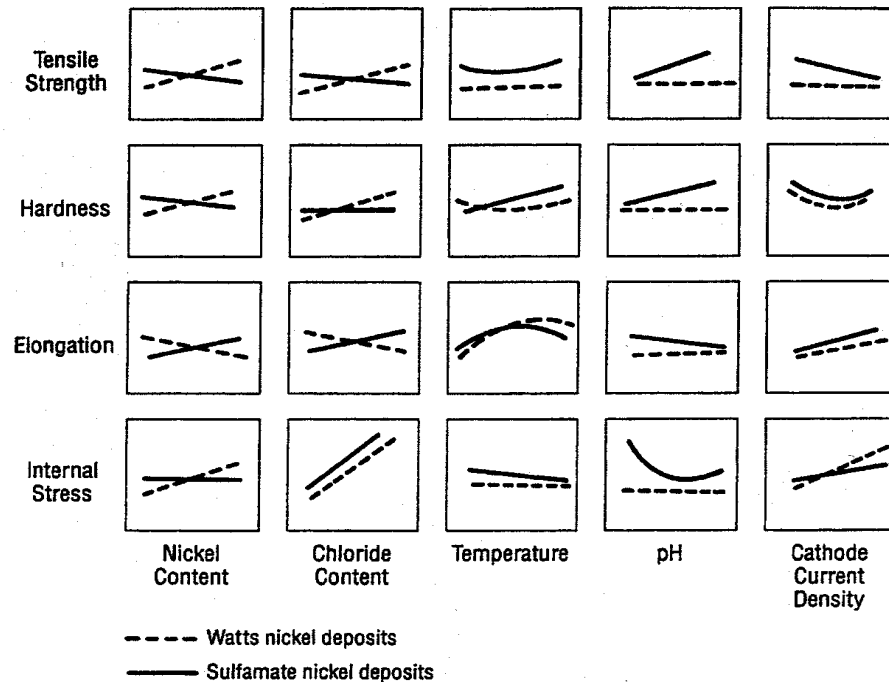


Figure 3-2 Qualitative effects of operating conditions on the properties of nickel electrodeposited from Watts and sulfamate solutions

Internal stress in electrodeposited nickel varies over a wide range depending on solution composition and operating conditions. Films resulting from sulfamate baths display a lower range of stress compared to Watts nickel, as shown in Table 3-3.

Table 3-3 Nickel Electroplating Solutions

	Electrolyte Composition (g liter ⁻¹)	
	Watts Nickel	Nickel Sulfamate
Nickel Sulfate	225-400	
Nickel Sulfamate		300-450
Nickel Chloride	30-60	0-30
Boric Acid	30-45	30-45
Operating Conditions		
Temperature (°C)	44-66	32-60
Agitation	Air or Mechanical	Air or Mechanical
Cathode current density (A dm ⁻²)	3-11	0.5-30
Anodes	Nickel	Nickel
pH	2-4.5	3.5-5.0
Mechanical Properties		
Tensile Strength (MPa)	345-485	415-610
Elongation (%)	10-30	5-30
Vickers Hardness (100g load)	130-200	170-230
Internal Stress (MPa)	125-185 (tensile)	0-55 (tensile)

Hydrogen, oxygen, carbon, sulfur, and chloride are the most common impurities present in nickel deposits that adversely influence the physical properties (density, resistivity) and the mechanical properties (tensile strength and ductility) with increasing concentration. The coatings obtained from sulfamate solutions operated at 49°C contain less carbon and sulfur than Watts nickel. According to the literature, the impurity content of the deposit from sulfamate solution has an inversely proportional relationship to the temperature of the bath, i.e. increasing the temperature reduces impurity concentration [34].

Safranek (1986) reports the modulus of elasticity of electroformed nickel ranging from 23,000 ksi to 30,800 ksi. The higher end of the spectrum corresponds to

nickel deposited in chloride baths or Watts baths with a high ratio of chloride and sulfate ions, whereas the low modulus values are associated with sulfamate solutions [34].

Electroplated nickel typically has a face-centered cubic (fcc) structure. Many nickel deposits exhibit a preferred crystal orientation with (100) planes parallel to the surface. The temperature and pH of a Watts electrolyte influences deposit crystal orientation. A high temperature of 75°C favors a (110) orientation. On the other hand, a randomly oriented deposit from a Watts bath develops a (100) orientation, at a pH of 2.1, and later a (211) orientation at a pH of 5.1 [34].

3.4.2 Process Quality Control

Quality control includes maintaining the concentrations of the main electrolyte constituents within specified limits, as well as preserving the purity of the electrolyte itself, controlling pH, temperature, and current density.

The basic components of the nickel electroplating solution that must be controlled are the nickel metal content, the chloride concentration, the boric acid level and the concentrations of the additional agents. Nickel metal concentration in the more common solutions can range between 22 and 46%. For instance, nickel sulfamate contains approximately 23.2% nickel [32]. It is desirable to have a minimum of 25 g liter⁻¹ nickel chloride in the solution to promote anode corrosion except when sulfur-activated electrolytic nickel anode materials are used.

The pH of nickel plating solutions increases during normal electroplating operation, thus small quantities of acid need to be added to keep it within range. Likewise, the operating temperature of the bath must be controlled to $\pm 2^\circ\text{C}$ of the

suggested value because temperature changes can have a significant impact on the properties of the nickel deposit.

The amount of time required to produce a certain nickel film thickness depends on the current density and the surface area to be covered. Estimates of the surface area to be plated should be made prior to initiating the electrodeposition to facilitate the monitoring process. Potentiostatic or voltage-controlled modes of operation are generally not encouraged. Maintaining a constant potential difference allows the current to fluctuate which has a negative effect on the uniformity of the plating, especially in the case of high aspect ratio microstructures. Instead, galvanostatic or current-controlled practices are recommended in order to meet minimum coating thickness requirements and to produce deposits with consistent and predictable properties.

Another aspect that should be controlled to promote the quality of the nickel deposit is the water used in manufacturing the plating solution. First of all the water should be deionized, especially if the local tap water has a high calcium content. Also, replacing the water lost by evaporation is important. As it happens any aqueous solution, water evaporation will lead to changes in concentration of the electrolyte followed by changes in pH, with the corresponding variations in deposit properties.

Inorganic, organic, and gaseous impurities may be introduced into nickel plating solutions during normal electroplating operation. Continuing efforts to eliminate these foreign substances can improve the nature of the electrodeposit. Filtering the electrolyte while depositing is frequently used to serve this purpose.

3.4.3 Parameters and Procedure

The solution of choice for the microfabrication process contained within is nickel sulfamate. This general purpose bath has a wide operating range, produces low stress deposits, and is easy to control. Other reasons supporting this preference have been reviewed in the previous subsections.

The bath is an aqueous nickel sulfamate solution prepared by mixing the appropriate components according to the proportions specified in Table 3-4 and adding deionized (DI) water until the total volume is 6 liters. Lauryl sulfate is added as a wetting agent, to increase the throwing power of the solution. Boric acid is the most commonly used buffering agent for nickel plating baths. It is effective in stabilizing the pH in the cathode film within the ranges normally required for best plating performance [32].

Table 3-4 Nickel Sulfamate Electroplating Bath Composition

Component	Chemical Formula	Quantity in Solution	Manufacturer
Nickel Sulfamate	$\text{Ni}(\text{SO}_3\text{NH}_2)_2$	2700 mL	Alfa Aesar, Ward Hill, MA
Boric Acid	H_3BO_3	225 g	Fisher Scientific, Fair Lawn, NJ
Lauryl Sulfate	$\text{C}_{12}\text{H}_{25}\text{O}_4\text{SNa}$	6 g	Sigma, St. Louis, MO

The nickel sulfamate anode utilized consists of sulfur-activated electrolytic nickel rounds (Belmont Metals, Brooklyn, NY) inside a titanium basket (Center for Microstructures and Devices, Baton Rouge, LA) encased in a cloth anode bag (Center for Microstructures and Devices, Baton Rouge, LA). The rounds have a unique shape

Substrate preparation preceding electroplating involved covering the areas where electrodeposition was not desired (i.e. the back-side of the substrate as well as some areas on the front) with Scotch Brand Tape (3M, St. Paul, MN).

The preliminary calculations required for the electrodeposition include estimates of the total area to be plated and the amount of time necessary to achieve a certain film thickness. The addition of appropriate specimen dimensions yielded a total surface area of 2.11 cm². The total current applied was determined by multiplying the current density times the surface area. Subsequently, using Equation (3.2), the time needed to produce the desired 400-micrometer thick nickel samples at a rate of 10 mA/cm², including a factor of about 10% overplating, necessary for uniform height of structures after lapping, was predicted to be approximately 36 hours.

The parameters used in the nickel plating process are listed in Table 3-5.

Table 3-5 Nickel Electroplating Parameters

Bath	Temperature	Operating Mode	Time	Current Density (mA/cm ²)	pH
Nickel Sulfamate	55°C	Galvanostatic	36 hours (calculated)	10	3.80-3.92

CHAPTER 4 SPECIMEN DESIGN AND FABRICATION

4.1 Specimen Configuration and Dimensions

The basic criteria utilized to establish specimen size and specific geometry consisted of the following:

- (1) Maximize the number of specimens per sample (substrate). Take advantage of the batch fabrication capability of LIGA to produce arrays of equally dimensioned specimens fabricated simultaneously.
- (2) Minimize or eliminate the need to handle the specimens after fabrication, thereby reducing the effect of associated disturbances and increasing the accuracy of results. The specimens were designed to measure fracture characteristics in pure tensile loading, which leads to opening or tensile failure mode, where the crack walls move directly apart from each other (Mode 1 crack displacement as seen in Figure 2-1). Thus, the specimens should not be subject to any bending or torsional loads before or during testing. The simplest way to eliminate specimen handling is preserving them attached to the wafer in some fashion. However, the specimens cannot remain completely attached to the substrate for the purpose of fracture testing, therefore, the use of a sacrificial layer in the fabrication process became inevitable. The fact that the specimens must be partially attached to the wafer also determined the almost complementary relationship between the sample and the testing mechanism.
- (3) Dimensionalize specimens based on “compact specimen” in ASTM standard E399 [30]. Due to the lack of standardization of mechanical

property testing in mesoscale, the specimen design followed a proportional reduction of the ASTM fracture toughness standard specimen dimensions to insure adequate mesosizes of specimen features (especially the notched area).

- (4) Design specimens to accommodate the testing mechanism. The mechanism employs a loading pin to apply the necessary force; hence, the specimens were designed with a corresponding perforation for this purpose. The use of a tension testing clevis was considered, as indicated in ASTM standard E399 for the testing of compact specimens [30]. However, the reasonable thickness limitations of the electrodeposited sacrificial layer did not allow for a sufficient gap to properly insert a clevis.

Figure 4-1 illustrates the layout of the specimens on the sample, including a scaling reference.

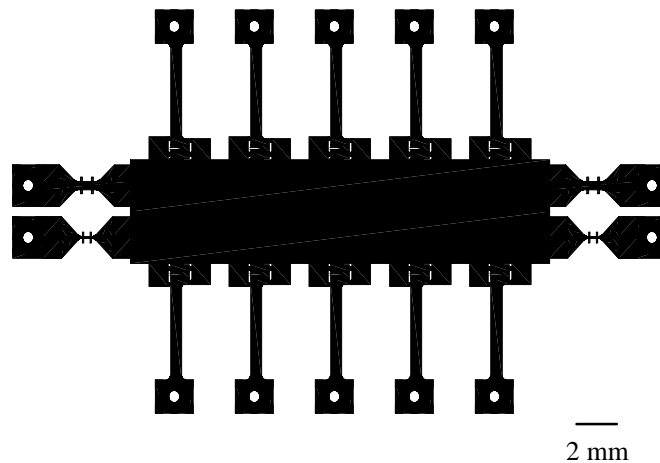


Figure 4-1 Specimen layout on sample (wafer)

The specimens have one end attached to a large mass or center block and their body is free-standing above the wafer with an opening at the unrestricted end, as described in part (d) above. The center block was intended to provide a large enough area to affix the specimens to the substrate and prevent them from detaching during testing. The size of the center block was estimated using a reasonable safety factor considering the total added area of all specimens and the electroplating current limitations. The pairs of dog biscuit-shaped tensile samples on the right and left side of the center block provide information on the maximum aspect ratio of the thick patterned photoresist, but mostly were included as test specimens for further developments on this research topic at a later date.

Figure 4-2 and Figure 4-3 display the configuration and dimensions of each individual fracture specimen, respectively.

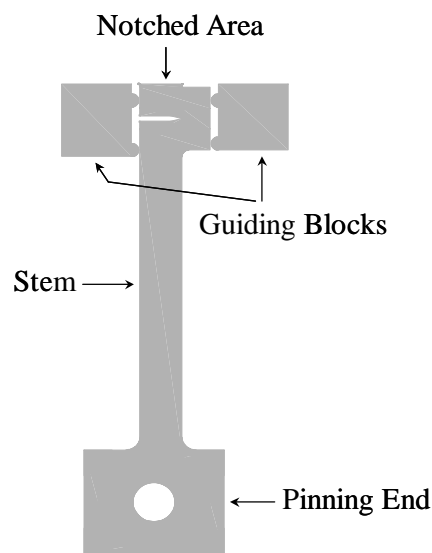


Figure 4-2 Fracture specimen configuration

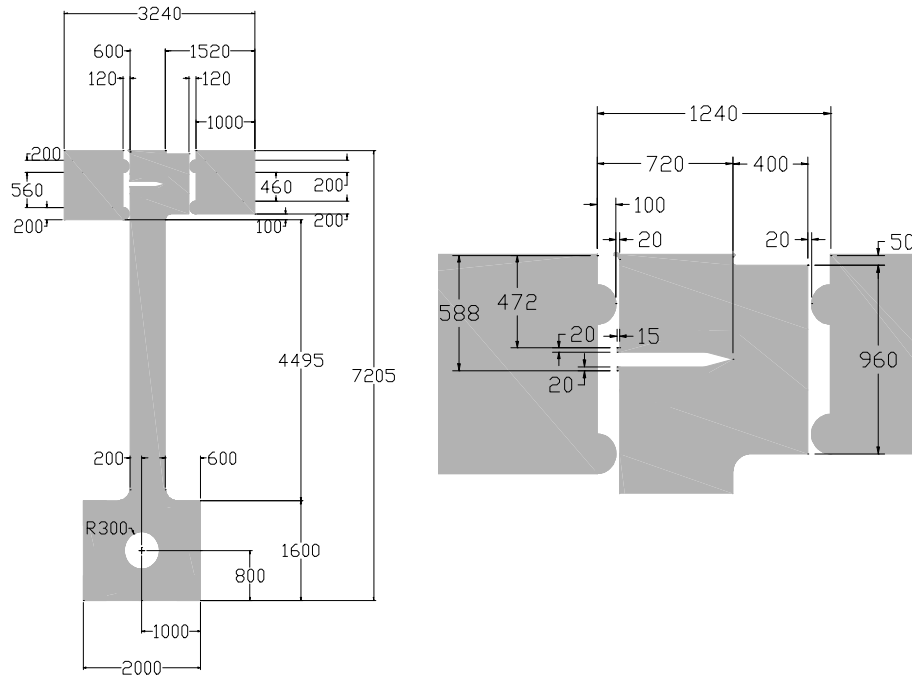


Figure 4-3 Fracture specimen dimensions (μm)

Each specimen is composed of a notched area, a pair of guiding blocks, a stem, and a pinning end. The notched area, located in the upper center of the specimen, is the most relevant part of it; this is the section where the fracture takes place. Giving rise to its name, this area was designed with a sharp notch in order to eliminate the Stage I fatigue growth (initiation) phase of the fracture process, as per ASTM E399 “compact specimen” design [30]. The notch is $600\mu\text{m}$ long and $76\mu\text{m}$ wide. The small protrusions at the outer edges of the notch were included for strain measurements, desirable in further developments on this research topic at a later date.

The notched area is bound to the left and right side by guiding blocks. The guiding blocks are simply rectangular masses each with two semicircular projections facing the notched area. These blocks were designed to further increase the accuracy of results by preventing any in-plane bending of the notched area during testing.

Specifically, the rectangular mass provides structural support to the semicircular projections intended to maintain the notched area in place during testing. The minimum distance between the guiding blocks and the notched area of the specimens is 20 μ m.

The stem is a long rectangular neck linking the notched area and the pinning end. The function of this piece is to provide a sufficient gap between the notched area (where the fracture takes places) and the point of force application, mainly for observation/recording purposes. The stem extends the point of force application a certain distance away from the notched area while maintaining the same line of force application as specified in the “compact specimen” design of ASTM E399 [30]. The length of the stem was determined by means of a simple beam deflection calculation, taking into account gravity and allowing for a deviation of up to 2 μ m. A safety factor of $\frac{1}{4}$ was included in the calculation. The width of this part is equivalent to the size of the opening in the pinning end.

The pinning end provides the point of contact between the specimen and the testing mechanism. It is composed of a rectangular mass with an opening for the loading pin, as described in part (d) above. The area around the puncture supplies structural support and keeps it attached to the specimen. The diameter of the opening was intended to reflect a reasonable value, compared to the overall specimen dimensions, considering the minimum sizes of commercially available loading pins. Similarly, the location of the perforation with respect to the notched area was designed in keeping with the specified line of force application for the loading pin [30].

4.2 Microfabrication

The microfabrication of the specimens subject of this research, which will be described in detail in the following pages, was performed at the J. Bennett Johnston Sr. Center for Advanced Microstructures and Devices (CAMD) and the Louisiana State University (LSU) Microsystems Muset Laboratory, in Baton Rouge, Louisiana.

4.2.1 Microfabrication Issues

Devising a suitable fabrication strategy involved experimenting with different techniques, and combinations thereof, to produce a final sequence deemed most appropriate for the research needs at that particular point in time. This course of action was critical to establishing the three major microfabrication steps involved (structural layer, sacrificial layer, and substrate), the details of which will be described below.

During the design stage of this project one of the key decisions made concerned the use of Ultra Violet (UV) lithography rather than X-ray lithography. At this point in time, X-ray mask fabrication was time-consuming, expensive, and unreliable, which shadowed the appeal of the LIGA technique. UV-LIGA is a modified LIGA technique in which certain photoresists (such as AZ-400 series and SU-8) are patterned using a near-UV light source. In contrast to X-ray masks, UV-mask fabrication was fairly simple. Also, UV-LIGA offered the possibility of employing alternative substrates, and the flexibility of microstructure geometry, which, furthered by the accessibility of a near-UV radiation source, suggested it was the most appropriate fabrication option at that particular moment. The shortcomings of the UV-LIGA technique are, mainly, the minimum feature size and resolution.

In the realm of UV-LIGA the choice of structural layer is reduced to either a positive UV-photoresist or a negative UV-photoresist. In most cases, positive photoresists yield a structural height ranging from the sub-micrometer level to a few tens of micrometers. On the other hand, SU-8 (MicroChem Corp., Newton, MA), which is a negative-tone, epoxy-based photoresist, can produce structural heights of several hundred micrometers. In fact, the literature reports SU-8 structures as thick as 2 millimeters with aspect ratios of 20 [38-39]. Thus, SU-8 was selected to fabricate the structural layer of the samples.

Three different sacrificial layer options were explored in combination with the SU-8 structural layer. Two of the options were UV-photoresists (negative and positive) and the last alternative was one of the more common sacrificial layer metals (copper). Information on the problems encountered in each case is given in Table 4-1 below. The electroplated copper sacrificial layer proved to be the most fitting solution.

Table 4-1 Sacrificial Layer Selection

Structural Layer	Sacrificial Layer	Issue	Viability of Combination
	SU-8	Very difficult to remove. Cannot insure proper releasing of structures.	No
SU-8	AZ4620 (Clariant Corp., Somerville, NJ)	Positive resist is not compatible with SU-8. Solvent in AZ diffuses into SU-8 during pre-baking amalgamating the films.	No
	Electroplated Copper	None. Good combination as long as selective copper-etch is used.	Yes

Initially, a thin nickel plate (Alfa Aesar, Ward Hill, MA) was utilized as a substrate in order to take advantage of the strong nickel-to-nickel bond when electrodepositing the specimens. Nevertheless, fabrication of the specimens on the nickel plate was unsuccessful due to the poor adhesion between it and the SU-8 resist. Evaporation of thin metallic layers on nickel, specifically chromium and gold, has been demonstrated to improve the adhesion between the substrate and the resist [40]. Chromium adheres well to nickel and gold serves to bond it to the SU-8. However, this defeats the original purpose of the nickel substrate (to draw on the strength of the nickel-to-nickel bond after electrodeposition), unless a metal etching step is incorporated in the fabrication procedure. Additionally, the chemicals contained in solutions that remove chromium and gold usually attack copper. The next logical choice was the standard substrate used for microfabrication purposes at CAMD and LSU: 4 inch-diameter single crystal silicon wafers (Silicon Inc., Boise, ID). These wafers are very lightweight and they conveniently adapt to microfabrication equipment. But, the fragile nature of these thin substrates (500 μ m) rendered them ineffective for the needs of this project. The chemical removal of the SU-8 as well as the mechanical polishing of the copper sacrificial layer seemed to be particularly severe on the structural integrity of the substrate, and resulting fracture was almost unavoidable. Usually, prior to reaching the nickel electroplating phase of the fabrication process only a small functional piece of the sample remained. Finally, the introduction of 4-inch diameter ceramic (alumina) disks (Laser Processing Technology, Portland, OR) proved to remedy the silicon substrate problems. The ceramic wafers were twice as thick as the silicon wafers;

consequently, they endured the processing challenges without fracturing while still maintaining similar advantageous qualities.

4.2.2 UV Mask Fabrication

Three optical masks (Nanofilm, Westlake Village, CA) were required based on the sample design using SU-8 as a structural layer, copper as sacrificial layer, and the UV-LIGA technique. Each positive-tone mask consisted of a 5-inch by 5-inch soda lime glass substrate coated with 1000 Å of chromium and 1µm of AZ 1518 positive UV-photosensitive. The mask patterns were created based on guidelines provided by Photo Sciences Inc. (St. Torrance, CA) to aid in the conversion of an AutoCAD drawing to a binary format that could be fractured into data read by the GCA Mann 3600 Optical Pattern Generator (OPG), (GCA Corp., Burlington, MA). The fractured data could be viewed in the PGCAM software (Artwork Conversions Software Inc., Santa Cruz, CA) before printing the UV mask to ensure that output to the OPG was acceptable. The GCA Mann 3600 has a high-pressure mercury arc lamp illumination source that is able to print a 4µm minimum feature size with a 0.1µm accuracy.

The sacrificial layer was patterned with a very basic design on a positive-tone mask, as shown in Figure 4-4. On the other hand, the design of the structural layer contains abundant intricate detail, as seen in Figure 4-1, hence it required the use of a negative-tone mask. At the point in time when the optical masks were produced, the method for fabricating negative-tone masks at CAMD entailed the removal of the AZ 1518 film from a positive-tone mask by means of flood-exposure. Subsequently, the chromium covered glass mask was placed in the Branson RF Plasma Asher (Branson International Plasma Corp., Hayward, CA) for 2 minutes at 600W in order to clean the

substrate of any film residue. Afterward, HR200, negative photoresist (Olin Microelectronics Materials, Norwalk, CT), was spin-coated on the substrate using the PWM 103 Heavy Duty Spinner (Headway Research Inc., Garland, TX) at 2000 rpm for 30 seconds and then pre-baked at 95 °C for 1 hour to evaporate the solvent. The process of printing the negative mask was called tone inversion, mainly because it required a previously OPG printed positive version of the same mask as a stencil to be used in the Oriel 6293 UV light source (Oriel Corp., Stratford, CT) for printing the negative mask. After exposing the negative mask for 1 second at 21-25 mW/cm² it was ready for development.

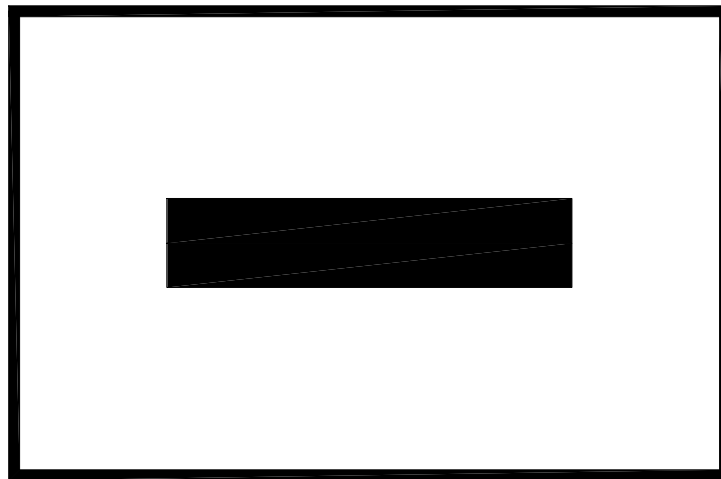


Figure 4-4 Sacrificial layer UV-mask design

Following the appropriate patterning of each mask, the positive masks were developed in Microposit 354 developer (Shipley Company, L.L.C., Malborough, MA) and the negative mask was developed in WNRD negative developer (Arch Chemicals Inc., Norwalk, CT). The developing time for each mask was determined by visual inspection based on the amount of areas being developed and the age of the developing chemicals. Typically, development for the positive mask took approximately 2 to 3

minutes and the development for the negative mask took approximately 6 to 7 minutes, with gentle agitation. The positive masks were then rinsed in DI water for about 3 minutes to remove the residue and the developer. The negative mask was soaked in Isopropanol (IPA) for nearly 7 minutes before following the same DI water rinse previously described.

For both negative and positive masks, cleansing and chromium etching followed the development process. In order to promote uniform etching of the chromium layer it is necessary to eliminate any film residue, particularly the adhesive coating between the photoresist and the chromium. This was performed by means of oxygen plasma with the Branson RF Plasma Asher (Branson International Plasma Corp., Hayward, CA) for 1 minute at 400W. Lastly, commercially available chromium etch (Olin Microelectronics Materials, Norwalk, CT), which consists primarily of nitric acid, was utilized to wet etch the thin metal layer underneath the photoresists. Again, the chromium etching time was established by visual examination with the aid of a microscope (Nikon Optiphot-88), such that when the metal layer was fully etched the glass substrate became optically transparent. The wet etching time, on average, was between 1 ½ to 3 minutes with gentle agitation. The finished masks were then rinsed in DI water for about 3 minutes to remove the chemicals and prevent under-etching.

4.2.3 Substrate Cleaning and Preparation

A 4-inch diameter alumina wafer (Laser Processing Technology, Portland, OR) was employed as a substrate for reasons discussed in Section 4.2.1 of this text. The ceramic disk was first thoroughly cleaned by successive rinsing in Acetone, IPA, and DI water, for approximately 3 minutes each time, followed by a blow-dry method using

nitrogen gas. The next step targeted the removal of moisture via dehydration in the M326 Mechanical Convection Oven for 20 minutes at 120 °C. Finally, the wafer was placed in the Branson RF Plasma Asher (Branson International Plasma Corp., Hayward, CA) for 10 minutes at 500W to further remove any chemical residue and promote good adhesion between the substrate and the films deposited subsequently.

The concluding phase of the substrate preparation was concerned with the deposition of two thin metal films, the first of which served to bond the substrate to the consecutive electroplating base metal. Specifically, 100 Å of chromium and then 1000 Å of gold were physically evaporated onto the alumina disk with a Temescal Model BJD-1800 E-beam Evaporator (BOC Edwards, Wilmington, MA) at a rate of 1 Å/sec and 5 Å/sec, respectively.

4.2.4 SU-8 Negative Photoresist

The photoresist of choice for both the sacrificial layer and the structural layer was SU-8 (MicroChem Corp., Newton, MA). The most attractive feature of this photoresist, especially for the purpose of this project, is its ability to produce up to 700µm thick layers in a single spin-coat with high aspect ratios. This negative photoresist is available in designations of 5, 10, 25, 50, and 100, reflecting the increasing degrees of viscosity necessary to achieve thicker coatings. The targeted height of the sacrificial layer was 90µm and that of the structural layer was 400µm, hence SU-8 25 was used in the first case and SU-8 100 in the latter instance. The films were achieved by dispensing dollar-size portions of the aforementioned photoresists on the wafer and spin-coating with the Light Duty Spinner (Headway Research Inc., Garland, TX).

Given all the positive functional aspects of SU-8, nevertheless, it proved to be rather sensitive to diverse applications, designs, substrates, and sacrificial layers. Consequently, all of the processing parameters were derived from the combined efforts of CAMD researchers and other CAMD users [37, 41-42]. Some application-specific tailoring of these parameters was required in order to generate an optimized and repeatable lithography procedure, particularly for the structural layer case.

The drawbacks of using this photoresist are primarily the large amount of residual stress in the resulting films, the height variations of the resist across the surface of the films, and the great difficulty to remove these coatings. There is a certain amount of stress inherent in the photoresist which, added to the stress induced during fabrication due largely to temperature changes and solvent diffusion, is clearly manifested through an abundance of microcracks on the surface of the coatings. In order to eliminate this phenomenon, periods of relaxation as well as increased cooling times were introduced at key stages of the fabrication process. In addition, the more viscous forms of SU-8 displayed considerable variations in height across the surface of the pre-baked films. This trend can be explained by the level-deviation of the surfaces used to pre-bake and/or post-bake the coatings. Ideally, the photoresist should be pre-baked and post-baked on perfectly flat surfaces. However, considering the fact that the metallic racks inside both of the Mechanical Convection Ovens experience constant thermal expansion and contraction, which sometimes leads to permanent deformation (warping), it is easy to appreciate how leveling these racks prior to processing helped but did not eliminate the problem. Using the M206 Mechanical Convection Oven available at CAMD yielded samples with less deviation in structural height as compared to those fabricated with the

M326 Mechanical Oven. Nonetheless, height variations of up to 100 μ m over the total area of the 400 μ m thick structural layer were recorded. Lastly, the issue of photoresist removal will be discussed in detail in the next section.

4.2.5 SU-8 Photoresist Removal

After UV-exposure and post-bake, SU-8 is a highly cross-linked functional epoxy, and as a result extremely difficult to remove, especially with conventional solvent based photoresist strippers. For instance, Nano Remover PG (MicroChem Corp., Newton, MA) will swell and lift off partially cross-linked SU-8, but will not remove hard baked (cured) SU-8.

According to information supplied by the company that manufactures the negative photoresist, dozens of SU-8 users have successfully developed stripping processes. Techniques include RIE plasma ashing, laser ablation, molten salt baths, CO₂ crystal and water jets and pyrolysis, among others. Particularly, at LSU and CAMD the most effective of the available stripping options at the point in time when the specimens subject of this research were fabricated, was chemical removal with Dynasolve 185 (Dynaloy, Indianapolis, IN). This product contains a blend of ingredients with an n-methyl pyrrolidone solvent base that facilitate polymer removal and prevent the redeposition of particles. Unlike its predecessor Dynasolve 165 (Dynaloy, Indianapolis, IN), Dynasolve 185 does not contain phenol, chlorinated solvents, or strong acids and bases, therefore it did not attack the copper or nickel present in the sample. Nevertheless, this method was not able to completely remove the exposed SU-8, especially the remains of the film present in very small, enclosed areas, even after sample immersion for 6-9 hours at 80-150 °C.

4.2.6 Copper Sacrificial Layer Etching

The fundamental concerns regarding the selection of the appropriate copper remover were selectivity and speed. Basically, the goal was to completely etch the 80-90 μ m thick copper deposit in a reasonable amount of time without attacking the nickel structures. Considering the limitations mentioned, identifying the right etchant to suit the needs of this project involved some experimentation. The stripping alternatives tested, and their corresponding outcomes are displayed in Table 4-2.

Table 4-2 Copper Etchant Selection

Name/Composition of Etchant	Issues		Prospect
	Speed	Selectivity	
20% Nitric Acid Solution	Fast. Rate is approx. 1.5 μ m/minute.	Not good	No
40% Concentrated NH ₄ OH and 60% DI water	Too slow. Rate is approx. 0.01 μ m/minute. Saturates very quickly.	Good	No
50% Concentrated NH ₄ OH and 50% Concentrated (30%) H ₂ O ₂	Too slow. Rate is approx. 0.01 μ m/minute. Saturates very quickly.	Good	No
C-38 Copper Stripper (Enthone, New Haven, CT)	Fast enough. Rate is approx. 1 μ m/minute. Saturates quickly, solution must be replaced once before fully etched.	Good	Yes

The commercially available C-38 Copper stripper (Enthone, New Haven, CT) was the etchant of choice based on the results obtained after testing the different copper removers. Figure 4-5 exhibits images of the nickel surface before and after stripping to demonstrate the selectivity of this etchant.

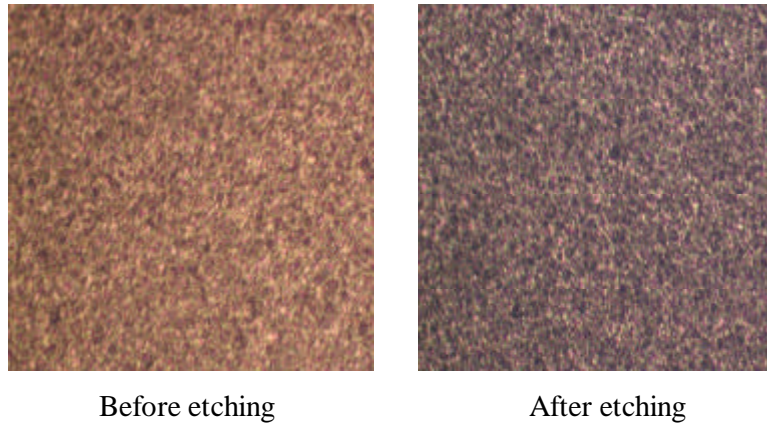


Figure 4-5 Nickel surface before and after copper etching (40X magnification)

4.2.7 Fabrication Sequence

The fabrication of the samples required three optical masks, two thick SU-8 layers, and two layers of electroplated metal. The fabrication procedure for the three optical masks and the substrate preparation are described in Section 4.4.2 and Section 4.4.3, respectively. The rest of the fabrication sequence (starting after the completion of the substrate preparation) is outlined below.

- (5) A thick film of SU-8 was spin-coated onto the wafer.
- (6) The SU-8 film was pre-baked to evaporate the solvent.
- (7) The film was gradually cooled to room temperature and relaxation of the film was accomplished.
- (8) The SU-8 was exposed with a near-UV light source using the mask shown in Figure 4-4.
- (9) Post-baking of the negative photoresist was done in order to induce cross-linking.
- (10) Prudent relaxation time for the film was granted.

- (11) The SU-8 film was developed in Nano SU-8 Developer (MicroChem Corp., Newton, MA).
- (12) Rinsing of the film in IPA and DI water was performed followed by blow-drying with nitrogen gas.
- (13) Film residue removal from the substrate was performed by means oxygen plasma.
- (14) The copper sacrificial layer was electrodeposited according to Section 3.3 of this text.
- (15) The sacrificial layer was manually and mechanically leveled to the height of the photoresist, followed by a DI water rinse and N₂ blow-dry.
- (16) The SU-8 coating was removed by means of immersion in a heated bath of Dynalove 185.
- (17) The remaining sacrificial layer and substrate were cooled to room temperature. Consecutive IPA rinsing and nitrogen gas blow-drying were performed.
- (18) The substrate was placed in an oxygen plasma source to eliminate film residue and promote adhesion between the sacrificial layer and the subsequent SU-8 film.
- (19) An ultra-thick structural layer of negative photoresist was spin-coated onto the sacrificial layer.
- (20) The unbaked film was allowed to relax for a sufficient amount of time.
- (21) The film was then pre-baked to remove the solvent.

- (22) Gradual cooling of the SU-8 to room temperature and relaxation of the film was accomplished.
- (23) The SU-8 was exposed with a near-UV light source utilizing the negative UV-mask based on the design of Figure 4-1.
- (24) Post-baking of the negative photoresist was done in order to induce cross-linking.
- (25) The film was again allowed to cool and relax for a sufficient amount of time.
- (26) The SU-8 film was developed in Nano SU-8 Developer (MicroChem Corp., Newton, MA) until a sharp, yet not overdeveloped, pattern was revealed.
- (27) Rinsing of the film in IPA and DI water was performed followed by blow-drying with nitrogen gas.
- (28) Film residue removal from the substrate was performed by means oxygen plasma.
- (29) The nickel structures were electrodeposited according to Section 3.4 of this text.
- (30) Mechanical leveling and polishing of the metal structures was carried out.
- (31) An attempt to dispose of the SU-8 structural layer was executed via immersion in a heated bath of Dynalove 185.
- (32) Specimen release was achieved by wet etching of the copper sacrificial layer.
- (33) Removal of the remains of the SU-8 structural layer was attempted by means of immersion in a heated bath of Dynalove 185.

The processing parameters associated with the fabrication steps indicated above for the sacrificial layer are shown in Table 4-3.

Table 4-3 Processing Parameters for Sacrificial Layer

Fab. Step	Parameters					Equipment used
	Time	Temp. (°C)	rpm	Energy /Power	Targeted thickness (µm)	
1	20 sec.		680		90	Light Duty Spinner (Headway Research Inc., Garland, TX)
2	1 ½ hr.	96				326 Mechanical Convection Oven
3	overnight	8/min.				326 Mechanical Convection Oven
4	26 sec.			480 mJ/cm ²		Oriel 6293 UV light source (Oriel Corp., Stratford, CT)
5	30 min.	96				326 Mechanical Convection Oven
6	overnight	8/min.				326 Mechanical Convection Oven
7	~ 11-16 min.					6' VA Polypropylene Chemical Hood
8	~ 3 min.					
9	~ 5 min.	65		300 W		Branson RF Plasma Asher (Branson International Plasma Corp., Hayward, CA)
10	9.9 hrs.	Room			99	See Section 3.3
11	~ 1 hr.					
12	½-1 hr.	80-150				6' VA Polypropylene Chemical Hood and Corning PC-220 Lab Stirrer/Hot plate
13	overnight	10/min.				6' VA Polypropylene Chemical Hood

The processing parameters associated with the fabrication order indicated above for the structural layer are displayed in Table 4-4.

Table 4-4 Processing Parameters for Structural Layer

Fab. Step	Parameters					Equipment used
	Time	Temp. (°C)	rpm	Energy /Power	Targeted thickness (µm)	
14	~ 5 min.	65		250 W		Branson RF Plasma Asher (Branson International Plasma Corp., Hayward, CA)
15	60 sec.		550		400	Light Duty Spinner (Headway Research Inc., Garland, TX)
16	overnight					Pre-leveled flat surface
17	5 hrs.	96				206 Mechanical Convection Oven
18	overnight	8/min				206 Mechanical Convection Oven
19	121 sec.			2783 mJ/cm ²		Oriel 6293 UV light source (Oriel Corp., Stratford, CT)
20	30 min.	70				206 Mechanical Convection Oven
21	overnight	8/min				206 Mechanical Convection Oven
22	~ 53-60 min.					6' VA Polypropylene Chemical Hood
23	~ 3 min.					

The processing parameters associated with the sequence indicated above for the final fabrication steps are exhibited in Table 4-5.

Table 4-5 Processing Parameters for Final Fabrication Steps

Fab. Step	Parameters					Equipment Used
	Time	Temp. (°C)	rpm	Energy /Power	Targeted thickness (μm)	
24	~ 5 min.	65		300 W		Branson RF Plasma Asher (Branson International Plasma Corp., Hayward, CA)
25	~ 36 hrs.	55			440	See Section 3.4
26	~ 2-3 hrs.					Hyprez Lapping Systems (Engis Corp., Wheeling, IL)
27	6 hrs.	80-150				6' VA Polypropylene Chemical Hood and Corning PC-220 Lab Stirrer/Hot plate
28	~ 4 hrs.	Room				6' VA Polypropylene Chemical Hood and Corning PC-220 Lab Stirrer/Hot plate
29	3 hrs.	80-150				6' VA Polypropylene Chemical Hood and Corning PC-220 Lab Stirrer/Hot plate

A schematic diagram of the fabrication sequence is shown in Figure 4-6.

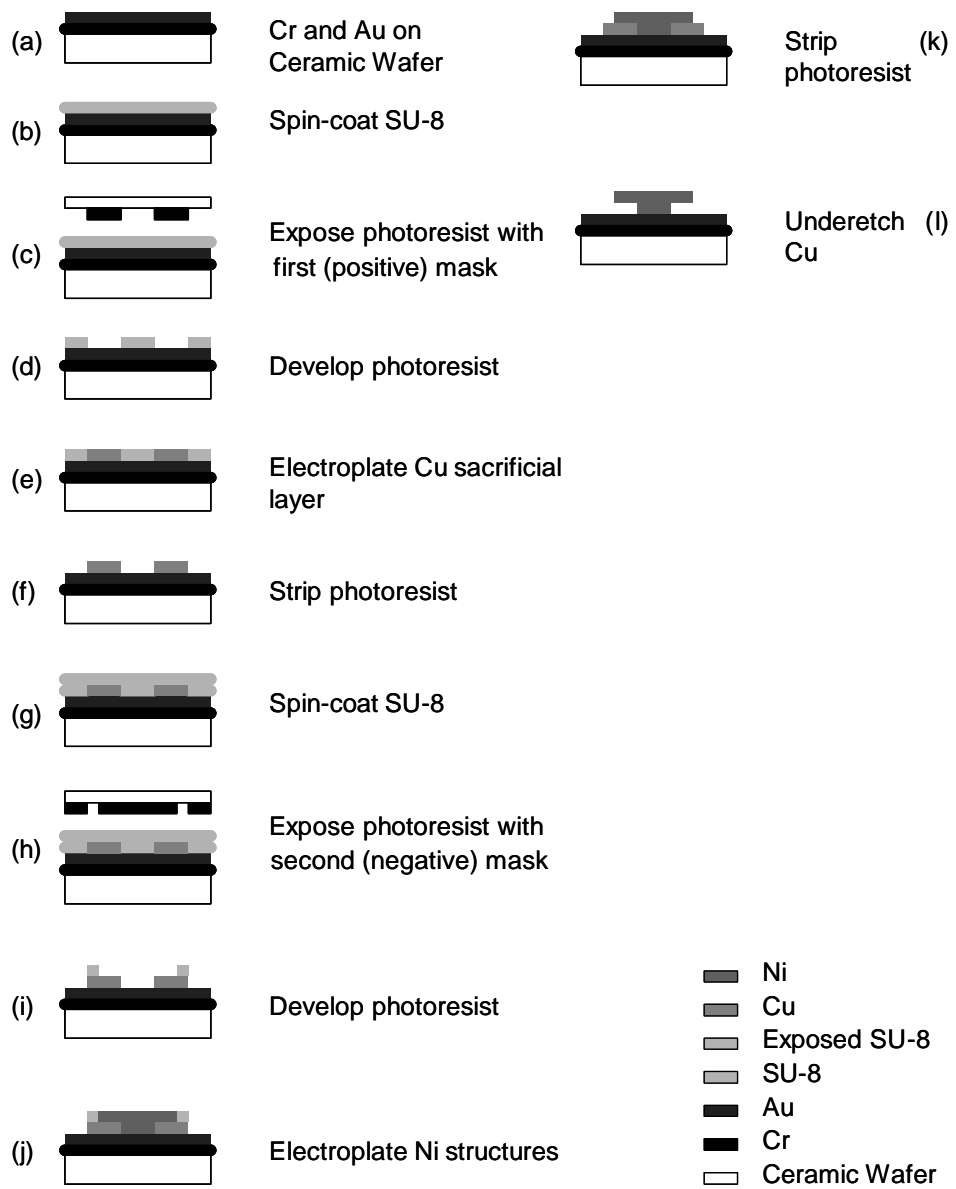


Figure 4-6 Schematic of sample fabrication sequence

CHAPTER 5 TESTING MECHANISM

5.1 Description of the Testing Mechanism

The testing mechanism can be divided into three distinct assemblies according to the functions performed: (a) motion and loading, (b) measuring and recording, and (c) fastening. The motion and loading assembly consisted of a model 200B air bearing with modified slider (Nelson Air Corp., Milford, NH), a PM500-C precision motion controller (Newport Corp. Irvine, CA), a loading pin arm (Mechanical Engineering Machine Shop, Baton Rouge, LA), a Prima 3-jaw drill chuck (Rohm Products of America, Lawrenceville, GA), and a pin gage (Vermont Gage, Swanton, VT). The measuring and recording assembly was comprised of an MDB-25 load cell (Transducer Techniques Inc., Temecula, CA), the Wafer Analysis System (WAS) software (CAMD, Baton Rouge, LA), a Dell Optiplex GM⁺ 5133 computer (Dell Computer Corp., Round Rock, TX), a regulated DC PR-18 power supply (Kenwood LTD., Long Beach, CA), a PCMCIA-232 data acquisition card (DAC) (National Instruments, Austin, TX), and Plug-n-Play General Purpose Interface Bus (GPIB) (National Instruments, Austin, TX). Lastly, the fastening assembly contained a vacuum chuck (Mechanical Engineering Machine Shop, Baton Rouge, LA), a substrate anchoring device (ATM Inc., Baton Rouge, LA), and a GAST model DOA-P104-AA vacuum pump (GAST Manufacturing Inc., Benton Harbor, MI).

Table 5-1 indicates the composition of each assembly along with the specific purpose of each part and their relevant specifications.

Table 5-1 Breakdown of Testing Mechanism

Assembly	Component	Purpose	Relevant Specifications
Motion and Loading	Model 200B air bearing	Eliminate friction in load applying process while coupling vacuum chuck to motion controller	
	PM500-C precision motion controller	Provide precise and accurate displacement in 4 axes (x, y, z, a)	15 nm resolution
	Loading pin arm	Connect drill chuck to a-axis of motion controller	
	Prima 3-jaw drill chuck	Hold loading pin in place	
	Pin gages	Apply load	540 μ m diameter
Measuring and Recording	MDB-25 load cell	Measure the applied load and output a corresponding voltage signal	Range: 0-25 lbs. Accuracy: 0.0125 lbs.
	WAS software	Provide computer based user interface for testing	
	Dell Optiplex GM ⁺ 5133 computer	Store the force and displacement data	
	DC PR-18 power supply	Provide excitation voltage for load cell	10 V
	PCMCIA-232 data acquisition card	Collect the output data from load cell and transfer the interpreted data to computer.	
	GPIB	Standard interface for communication between computer and motion controller	
Fastening	Vacuum chuck	Affix sample to air bearing	
	Vacuum pump	Provide the vacuum pressure	~ 650 mmHg
	Anchoring device	Aid in restraining sample movement	

An illustration of the most mechanically significant elements of the testing setup and their corresponding arrangement is provided in Figure 5-1.

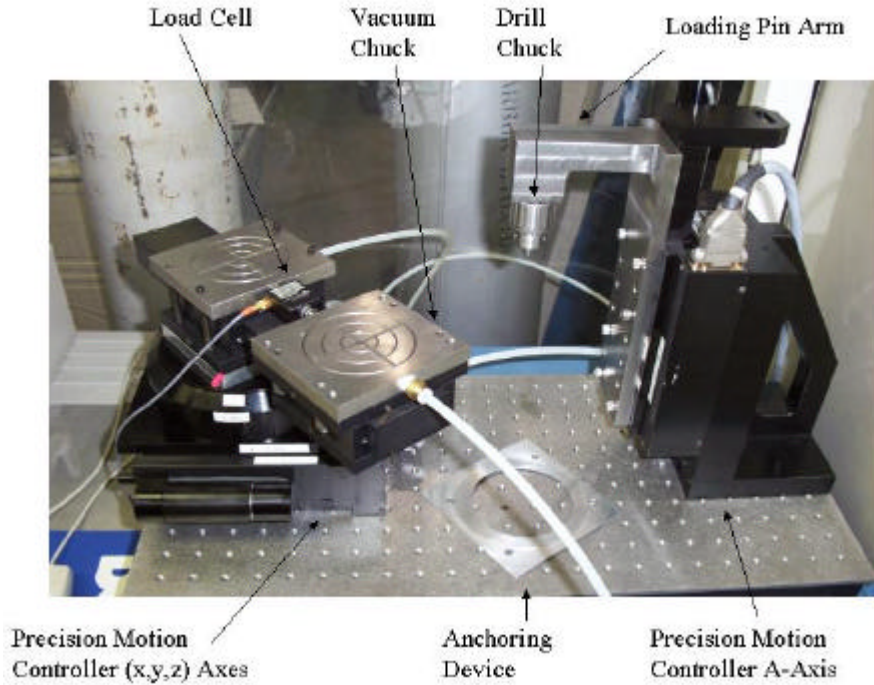


Figure 5-1 Fundamental mechanical elements of the testing setup

Based on the configuration of the testing mechanism, the user had the ability to give displacement commands and to instruct the commencement of the actual fracture experiment and the associated measurement recording. The displacement commands were channeled to the GPIB and then to the motion controller to execute the request. Consequently, the motion controller furnished coordinate information back to the GPIB and finally to the user through the WAS software. Likewise, the instant that measurement recording was dictated, the DAC supplied the data to the computer which in turn stored it for further user viewing. The basic flow of information through the testing mechanism is described diagrammatically in Figure 5-2.

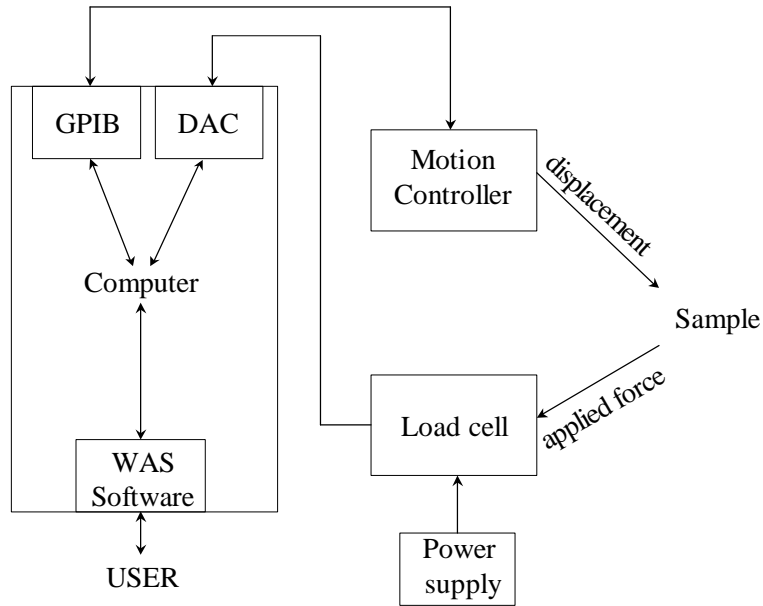


Figure 5-2 Testing mechanism information flow diagram

5.2 Testing Procedure

The testing method used for the fracture specimens was very straightforward. Basically, the x, y, z, and a axes were used to position the loading pin in the corresponding opening of the pinning end of the specimen. The x, y, and z axes directed the sample movement; the x-axis spanned forward and backward, the y-axis extended left and right, the z-axis spanned counter-clockwise and clockwise rotation. The a-axis shifted the loading pin arm up and down. Subsequently, the pin was lowered into the opening, by a negative displacement in the a-axis, until it was in contact with the ceramic substrate. The pin was then lifted a few micrometers above this position in order to prevent friction between the loading pin and the substrate. Finally, the actual fracture experiment was carried out by fixing the loading pin arm (a-axis), as well as the x and z axes, and slowly displacing the y-axis in the positive direction until

complete fracture occurred. During this last stage the load cell output (mV reading and force in pounds), and y-axis displacement in micrometers, were recorded.

5.3 Testing Related Calculations

In view of the testing mechanism and the nature of the test itself, estimates of the amount of force necessary to fracture the specimens, the amount of force application induced bending on the loading pin, and the total membrane deflection produced by the vacuum pump on the substrate, were significant design considerations addressed as follows.

The fracture force required was approximated using Equation (5.1), assuming a maximum 400-micrometer thickness of the specimens and the ultimate tensile strength of bulk nickel, σ_{ult} , namely 317 MPa.

$$s_{ult} = \frac{F}{A} \quad (5.1)$$

where F is the required force and A is the area over which the force is applied, in this case, the difference between the width of the specimen and the notch area.

Applying Equation (5.1) with the nominal 600-micrometer notch length a load of 17.10 lbs. resulted. Thus, after adding a safety factor of 40%, it was determined that the load required to exceed the ultimate tensile strength of the specimens was about 24 lbs. Based on this information and the commercially available load cells, the best choice was that which ranged between 0-25 lbs.

In order to find the bending induced on the loading pin during testing, a cantilever beam case with one end fixed, the other end free, and a point load applied a certain distance from the free end, was assumed [43]. First of all, the moment of inertia,

I , of the loading pin was calculated taking into account the pin diameter (540 μm) and using Equation (5.2).

$$I = \frac{P}{4} D^4 \quad (5.2)$$

where D is the diameter of the loading pin.

In this fashion, the moment of inertia was estimated to be $1.60 \times 10^{-7} \text{ in}^4$. Next, the maximum deflection of the pin was assessed by employing Equation (5.3).

$$y = \frac{W}{6EI} (2l^3 - 3l^2a + a^3) \quad (5.3)$$

where y is the maximum deflection, W is the point load, E is the Young's Modulus value, l is the length of the pin, and a is the distance at which the load is applied from the free end of the pin.

According to manufacturer's specifications the loading pin has a Young's Modulus of 29000 ksi. The total length of the pin was assumed to be 2 millimeters and the load was assumed to be applied at the top surface of the specimen with the pin's free end suspended $5\mu\text{m}$ above the substrate. Based on these premises, Equation (5.3) yielded a value for the deflection of the loading pin of $9.61\mu\text{m}$. Similarly, the moment, M , exerted on the pin was computed as 1.003 lbs-in based on Equation (5.4)

$$M = W(l - a) \quad (5.4)$$

The resulting stress, σ_R , was then approximated using Equation (5.5) which yielded a numerical value of 62688 psi.

$$\sigma_R = \frac{Mc}{I} \quad (5.5)$$

where c is the half diameter dimension of the pin.

When comparing σ_R to the Shear Modulus value of the loading pin material, tabulated as 11200 ksi, it is evident that pin breakage during testing was not a major concern.

The physical consequence of the application of vacuum pressure on the underside of the ceramic disk while placed on the grooved vacuum chuck was best described by what the literature has termed as membrane or diaphragm-type deflection on solid, circular, simply supported plates with uniform loading [43]. As such, the plate constant, D , for the alumina disk was calculated first according to Equation (5.6) .

$$D = \frac{Et^3}{12(1-\nu^2)} \quad (5.6)$$

where E is Young's Modulus, t is the plate thickness, and ν is Poisson's Ratio.

The ceramic substrates were 1 millimeter thick and the values for E and ν were 53665 ksi and 0.22, respectively. Thus, Equation (5.6) produced a numerical result of 287.44 lb-in. Subsequently, a value for the maximum membrane deflection, y_m , was produced by utilizing Equation (5.7) in conjunction with a fundamental assumption regarding the unsupported radius of the disk.

$$y_m = \frac{qa^4(5+\nu)}{64D(1+\nu)} \quad (5.7)$$

where q is the gage pressure (i.e. the difference between the vacuum pressure and the atmospheric pressure), and a is the unsupported radius of the disk.

For the most part the substrate is well supported based on the vacuum chuck's concentric annular grooves design. The grooves are 1/16 inch thick. The section where the maximum deflection should occur was deemed to be that which involved the largest exposed or unsupported area. In this case that was the center of the vacuum chuck

where the feeding hole, that distributes the pressure to the grooves, possesses a radius of 0.25 inches, as exhibited in Figure 5-1. Additionally, a safety factor of 2 was used for the value of the unsupported radius of the disk so as to intentionally create a more critical scenario for substantiation of the design. Consequently, using a gage pressure of 110 mmHg and value of 0.5 inches for a , Equation (5.7) yielded a y_m value of 0.77 μm corresponding to an insignificant 0.08% deflection.

CHAPTER 6 RESULTS

This chapter presents experimental outcome for the UV-LIGA fabricated nickel fracture specimens. It includes an overview of the final fabrication product and preliminary fracture strength test results.

6.1 UV-LIGA Fabrication Results

Under the conditions and fabrication sequence outlined in Table 4-3 to Table 4-5 and Figure 4-6, the UV-LIGA process was successfully demonstrated to microfabricate suitable freestanding, wafer-bound specimens with two thick SU-8 negative photoresist layers and two layers of electrodeposited metal.

6.1.1 Dimensional Change

The WYKO NT-3300 Profiling System (Veeco Metrology Group, Tucson, AZ) available at CAMD was utilized to obtain measurement data on the fabricated specimens including thickness of specimens, width of notched area, notch length, and notch width.

Table 6-1 shows the percent deviation of measured values from the nominal design values for the some specimen dimensions.

Table 6-1 Relative Dimensional Change

Dimension	Nominal (μm)	Average of Actual (μm)	Percent Deviation (%)
Notch Length	600	576	-4
Notch Width	76	79	+4
Width of Specimen	1000	990.5	-0.95

These dimensional changes can be attributed to the fact that the SU-8 photoresist undergoes significant chemical changes during UV exposure, where the

photoinitiator generates an acid to facilitate the polymeric cross-linking, causing the photoresist to distend. The percentage deviations measured are consistent with the previously mentioned swelling effect and range from -4 to 4%.

On the other hand, the thickness of the specimens varied between 120 to 127 μm . This represents a 68-70% reduction of the final metal thickness as compared to the targeted 400 μm thick structural layer. This is not surprising considering the fact that SU-8 photoresist is largely sensitive to processing parameters, as mentioned previously in Section 4.2.4. Factors such as photoresist spin-coating, exposure, and development, are very likely to cause this phenomenon. Likewise, certain electrodeposition issues such as insufficient overplating and electrodeposition leakage (i.e. presence of deposit in undesired areas due to electrical isolation failure) can also contribute to thinner resulting metal thickness.

6.1.2 Nickel Specimen Electrodeposition

Figure 6-1 shows a Nikon MM-22U Measurescope image of a single UV-LIGA fabricated nickel specimen. The nickel deposition was smooth, shiny, and uniform. No apparent defects such as nodules in hole or burned deposits were visible.

6.1.3 Freestanding Nickel Specimens

The C-38 Copper Stripper formula used was demonstrated to effectively remove the copper sacrificial layer from the sample, therefore generating cantilever beam-like specimens suspended on the ceramic disk as displayed in Figure 6-2 and Figure 6-3.

6.1.4 SU-8 Removal

Additional experimentation is needed to determine the optimal solution to fully remove the negative photoresist for the current microfabrication procedure.

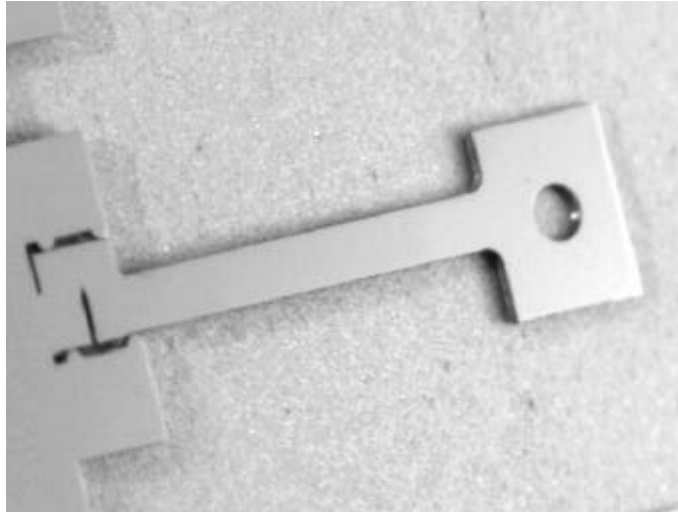


Figure 6-1 Single UV-LIGA fabricated specimen on alumina substrate

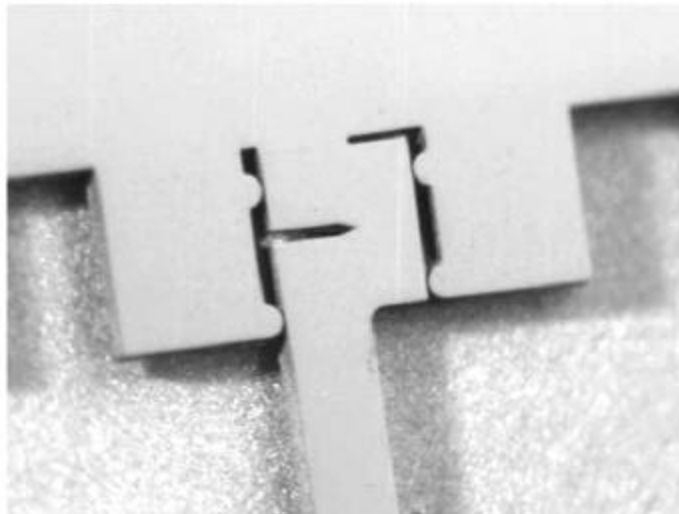


Figure 6-2 Measurescope image of single freestanding notch and guiding blocks revealing specimen sidewalls

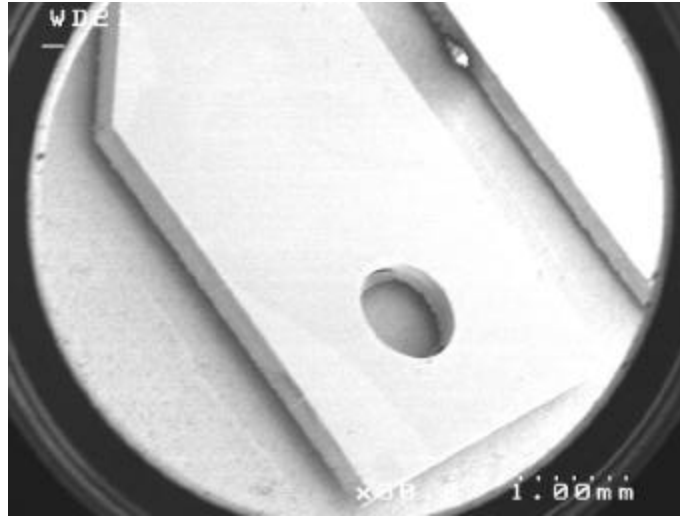


Figure 6-3 Partial Scanning Electron Microscope (SEM) image of tensile specimen enhancing the gap between the bottom of the nickel structure and the ceramic wafer

This might require not a single stripping technique but a combination thereof so as to eliminate even the microscopically visible remains. In view of the removing techniques available and the specific need of this project, full immersion in Dynasolve 185 for extended periods of time (> 6hrs.) at high temperatures (80-150 °) seems the most reasonable approach to eliminate the majority of the exposed SU-8 film. However, photoresist residue continues to be present in smaller enclosed areas as illustrated in Figure 6-4 and Figure 6-5. Plasma ashing could prove useful to purge this SU-8 residue. However, extensive sample surface oxidation caused by contact with the oxygen plasma should be considered.

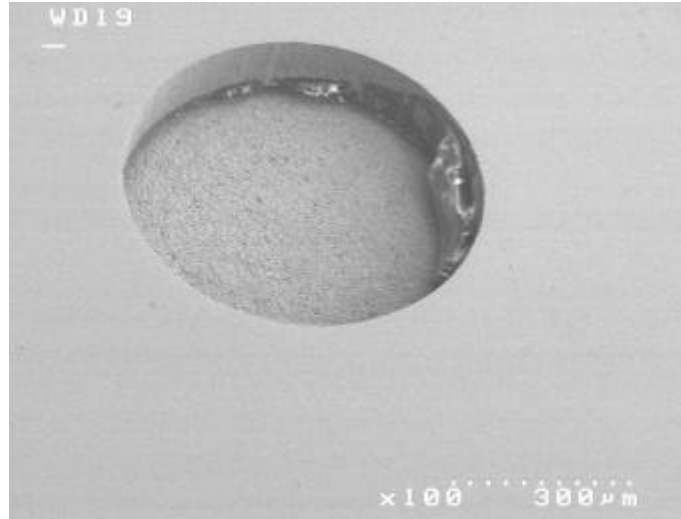


Figure 6-4 SEM image of perforation at pinning end of fracture specimen containing SU-8 residue

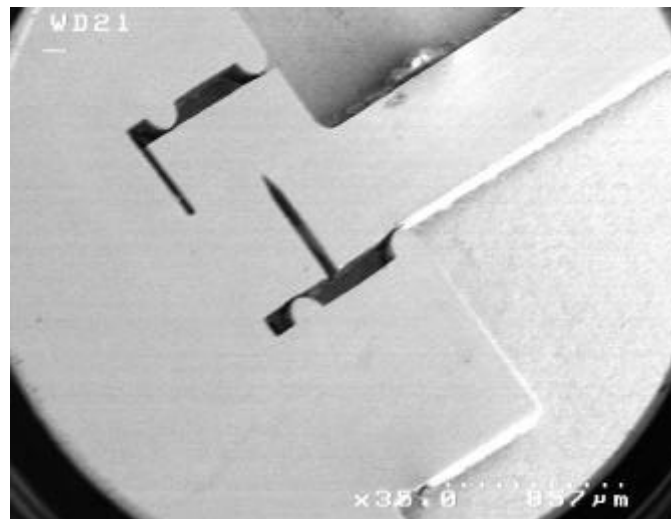


Figure 6-5 Partial SEM image of fracture specimen showing SU-8 remains on one side of the stem

6.2 Preliminary Fracture Testing Results

In order to validate the compatibility of the sample design and fabrication with the testing mechanism as well as ascertain the system's capability to perform the

required tests, a few specimens were run to complete fracture and the corresponding data was registered. Figure 6-6 below presents the force versus displacement test data obtained, where specimen 9 defines the curve trend and the remaining data reveals the maximum force sustained by each individual specimen.

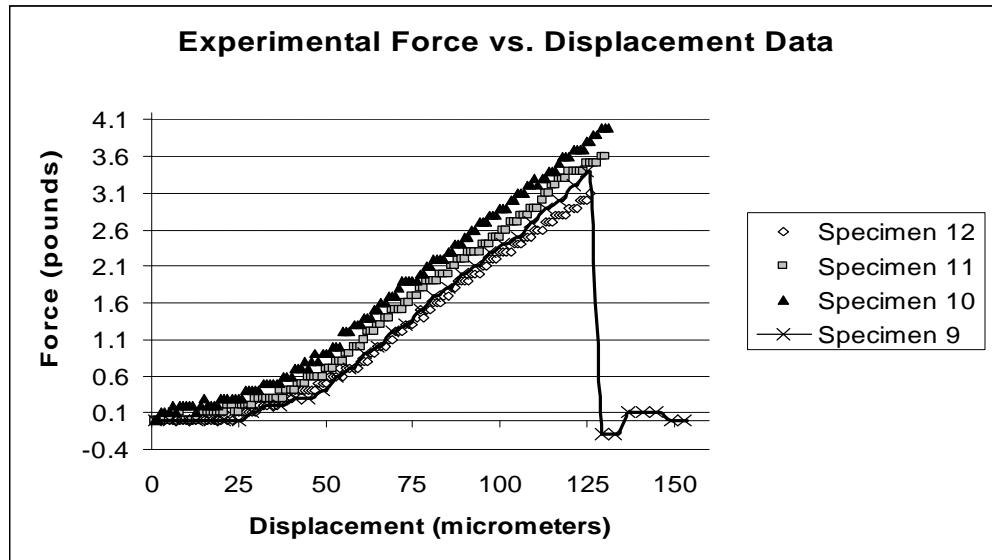


Figure 6-6 Force as a function of displacement with fracture force values represented for specimens 10-12 and trendline revealed by specimen 9

The strength values derived from the experimental information collected are displayed in Table 6-2. The average values are expressed with 95% confidence intervals. These values are a measure of the resistance-to-fracture of UV-LIGA fabricated nickel specimens based on the particular design, and under the specific electrodeposition conditions described in previous chapters of this text. Obtaining more data from both notched and unnotched (tensile) specimens becomes crucial to determine the precise implication of the experimental figures, mainly due to the limited availability of mesoscale material property values for notched microfabricated nickel specimens for comparison purposes.

Table 6-2 Fracture Strength Values for Specimens 9-11

Specimen Number	Maximum Load (N)	Fracture Strength (MPa)
9	15.12	304
10	17.79	358
11	16.01	322
12	13.79	277
AVERAGE	15.68 ± 2.67	315 ± 54
STANDARD DEVIATION	1.68	34

6.2.1 Fracture Surface

Figure 6-7 shows an SEM image of the total fracture surface of a nickel specimen.

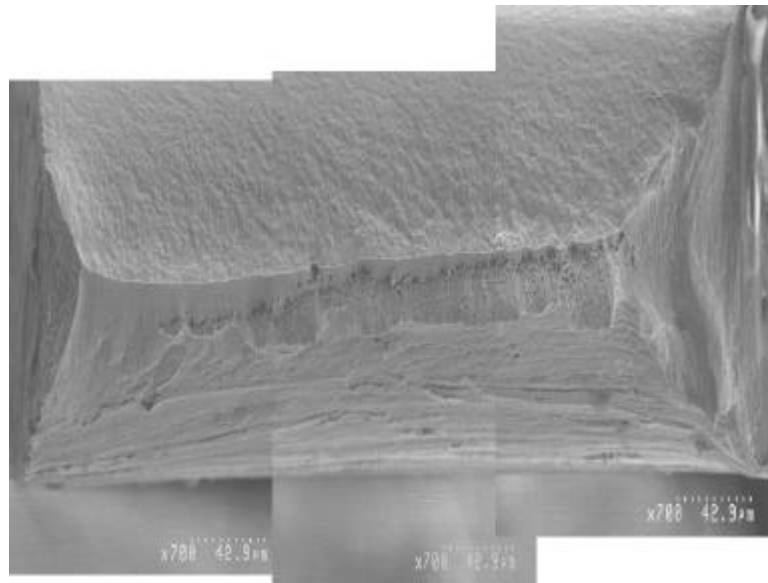


Figure 6-7 Stitched SEM image of the fracture surface of specimen 11

Due to the mesosize of the notch and the minimum magnification of the SEM several images had to be stitched together to capture the entire length of the fracture surface. Figure 6-7 reveals a considerable amount of plastic deformation (necking) preceding final failure and indicative of the ductility of the material. Additionally, the

fracture surface configuration seems to indicate a tearing fracture mode, therefore implying insufficient time for fully developing and propagating the crack.

The fracture information presented is just a graphic supplement to the testing outcome previously discussed. An elaborate materials characterization study including techniques such as Transmission Electron Microscopy (TEM) and hardness testing should be considered for further development of this research topic.

CHAPTER 7 SUMMARY AND RECOMMENDATIONS

This project lays the groundwork for the successive mass collection of microfabricated material property data such as resistance-to-fracture values. It emphasizes on the design and realization of the test specimens and testing mechanism as complimentary parts, according to the objectives of the research, to obtain material property data at the microscale.

The UV-LIGA processing method utilized successfully produced suitable freestanding, wafer-bound specimens. The devised testing mechanism demonstrated compatibility with the fabricated samples and capability of performing the desired experimentation by generating resistance-to-fracture values of the nickel specimens. Preliminary testing results proved that further data acquisition, especially involving tensile specimen testing, and material analysis is needed to fully understand the implications of the information obtained and to contribute useful figures to the lacking material property characterization bank for microfabricated structures. The products of this new microspecimen testing approach can be extended for use with other microfabricated metals and metal alloys, particularly on a more qualitative, comparative basis.

A few suggestions to improve or further the fabrication procedure include adding a plasma ashing step at the end of the sequence to attempt to eliminate the SU-8 residue, and increasing the amount of nickel overplating in order to obtain thicker nickel specimens

A portable, high magnification microscope with photographic functions, or a Charge Coupled Device (CCD) camera, could be a valuable accessory to the current

testing mechanism by adding strain measurement capabilities. Another improvement to the testing mechanism consist of developing a more exact method of perpendicularly positioning the a-axis and the y-axis during fracture testing to further insure the accuracy of results.

REFERENCES

- [1] Madou, M., *Fundamentals of Microfabrication*. CRC Press, Boca Raton, 1997.
- [2] Kraft, O., Schwaiger, R., and Nix, W.D., *Measurement of Mechanical Properties in Small Dimensions by Microbeam Deflection* in *Materials Research Society Symposium N: Microelectromechanical Structures for Materials Research Proc.* San Francisco, California: April 15-16, 1998. pp. 39-44.
- [3] Sharpe, W.N., Jr., Brown, S., Johnson, G. C., and Knauss, W., *Round-Robin Tests of Modulus and Strength of Polysilicon* in *Materials Research Society Symposium N: Microelectromechanical Structures for Materials Research Proc.* San Francisco, California: April 15-16, 1998. pp. 57-65.
- [4] Ballarini, R., et al., *The Fracture Toughness of Polysilicon Microdevices* in *Materials Research Society Symposium N: Microelectromechanical Structures for Materials Research Proc.* San Francisco, California: April 15-16, 1998. pp. 137-142.
- [5] Tsuchiya, T., et al., *Specimen Size Effect on Tensile Strength of Surface Micromachined Polycrystalline Silicon Thin Films* in *IEEE Tenth Annual International Workshop on Micro Electro Mechanical Systems Proc.* Nagoya, Japan: January 26-30, 1997. pp. 529-534.
- [6] Sharpe, W.N., Jr., Yuan, B., Jr., and Edwards, R.L., *A New Technique for Measuring the Mechanical Properties of Thin Films*. *J. of Microelectromechanical Systems*, 1997. 6,(3), pp. 193-198.
- [7] Van Arsdell, W. and Brown, S., *Subcritical Crack Growth in Silicon MEMS*. *J. of Microelectromechanical Systems*, 1999. 8,(3), pp. 319-327.
- [8] Lee, S.-H., et al., *Evaluation of Microfracture Toughness and Microcracking with Notch Tip Radius of Si Film Structure for Microactuator in Hard Disk Drives*. *Microsystem Technologies*, 2001. 7, pp. 91-98.
- [9] Pratt, R.I. and Johnson, G.C., *Multilayer Microelectromechanical Structures for Material Property Characterization* in *Materials Research Society Symposium N: Microelectromechanical Structures for Materials Research Proc.* San Francisco, California: April 15-16, 1998. pp. 15-20.

- [10] Dual, J., et al., *Mechanical Properties of Microstructures: Experiments and Theory* in *The International Society for Optical Engineering: Microlithography and Metrology in Micromachining III Proc.*: September, 1997. pp. 12-22.
- [11] Greek, S. and Ericson, F., *Young's Modulus, Yield Strength and Fracture Strength of Microelements Determined by Tensile Testing in Materials Research Society Symposium N: Microelectromechanical Structures for Materials Research Proc.* San Francisco, California: April 15-16, 1998. pp. 51-56.
- [12] Ballarini, R., Mullen, R.L., and Yin, Y., *The Fracture Toughness of Polysilicon Microdevices: A First Report.* J. of Mat. Res., 1997. 12,(4), pp. 915-922.
- [13] Wilson, C.J. and Beek, P.A., *Fracture Testing of Bulk Silicon Microcantilever Beams Subjected to a Slide Load.* J. MEMS, 1996. 5,(3), pp. 142-150.
- [14] Fitzgerald, A.M., Dauskardt, R.H., and Kenny, T.W., *Fracture Toughness and Crack Growth Phenomena of Plasma-Etched Single Crystal Silicon.* Sensors and Actuators, 2000. A83, pp. 194-199.
- [15] Suito, W. and Dunn, M., *Fracture Initiation at Sharp Notches in Single Crystal Silicon.* J. Appl. Physics, 1998. 83,(7), pp. 3574-3582.
- [16] Johansson, S., et al., *Fracture Testing of Silicon Microelements In Situ in a Scanning Electron Microscope.* J. Appl. Physics, 1998. 63,(10), pp. 4799-4803.
- [17] Sharpe, W.N., Jr., LaVan, D.A., and Edwards, R., *Mechanical Properties of LIGA-Deposited Nickel for MEMS Transducers* in *IEEE International Conference on Solid-State Sensor and Actuators Proc.* Chicago, Illinois: June 16-19, 1997. pp. 607-610.
- [18] Sharpe, W.N., Jr. and McAleavey, A., *Tensile Properties of LIGA Nickel* in *The International Society for Optical Engineering Conference on Materials and Device Characterization in Micromachining Proc.* Santa Clara, California: September, 1998. pp. 130-137.

- [19] Sharpe, W.N., Jr., LaVan, D.A., and McAleavey, A., *Mechanical Testing of Thicker MEMS Materials*. ASME J. of MEMS, 1997. DSC Vol. 62/HTD Vol. 354, pp. 93-97.
- [20] Mazza, E., Abel, S., and Dual, J., *Experimental Determination of Mechanical Properties of Ni and Ni-Fe Microbars*. Microsystem Technologies, 1996. 2, pp. 197-202.
- [21] Stephens, L.S., et al., *Mechanical Property Evaluation of Electroplated High Aspect Ratio Microstructures in Materials Research Society Symposium N: Microelectromechanical Structures for Materials Research Proc.* San Francisco, California: April 15-16, 1998. pp. 173-178.
- [22] Majjad, H., et al., *Dynamic Determination of Young's Modulus of Electroplated Nickel Used in LIGA Technique*. Sensors and Actuators, 1999. A74, pp. 148-151.
- [23] Shi, Q., et al., *Characterization of Electroformed Nickel Microstructures in The International Society for Optical Engineering: Micromachining and Microfabrication Process Technology Proc.*: September, 1995. pp. 191-199.
- [24] Christenson, T.R., et al., *Mechanical and Metallographic Characterization of LIGA Fabricated Nickel and 80% Ni-20% Fe Permalloy in Materials Research Society Symposium N: Microelectromechanical Structures for Materials Research Proc.* San Francisco, California: April 15-16, 1998. pp. 185-191.
- [25] Buchheit, T.E., et al., *Understanding and Tailoring the Mechanical Properties of LIGA Fabricated Materials in Materials Research Society Symposium AA: Materials Science of Microelectromechanical Systems (MEMS) Devices Proc.* Boston, Massachusetts: December 1-2, 1998. pp. 121-126.
- [26] Ruther, P., et al., *Prototype of a Microtesting System Made by the LIGA Process to Measure the Young's Modulus in Cantilever Microbeams*. ASME J. of Dyn. Syst., Measurement, and Control, 1997. 119, pp. 57-60.
- [27] Collins, J.A., *Failure of Materials in Mechanical Design - Analysis, prediction, Prevention*. Second ed. John Wiley & Sons, New York, 1993.
- [28] Dieter, G.E., *Mechanical Metallurgy*. Third ed. Materials Science and Engineering Series, McGraw Hill, Singapore, 1986.

- [29] Hertzberg, R.W., *Deformation and Fracture Mechanics of Engineering Materials*. Fourth ed. John Wiley & Sons, New York, 1996.
- [30] American Society for Testing and Materials, *Standard Test Method for Plain-Strain Fracture Toughness of Metallic Materials*, Desig.: E399, in *Annual Book of ASTM Standards*, Vol. 03.01, Philadelphia, 1998. pp. 506-534.
- [31] Mohler, J.B., *Electroplating and Related Processes*. Chemical Publishing, New York, 1969.
- [32] Schlesinger, M. and Paunovic, M., *Modern Electroplating*. Fourth ed. Electrochemical Society Series, John Wiley & Sons, New York, 2000.
- [33] Prentice, G., *Electrochemical Engineering Principles*. Prentice Hall International Series in the Physical and Chemical Engineering Sciences, Prentice Hall, New Jersey, 1991.
- [34] Safranek, W.H., *The Properties of Electrodeposited Metals and Alloys*. Second ed. American Electroplaters and Surface Finish Society, Orlando, 1986.
- [35] Sarad, R., Henry Leidheiser, J., and Ogburn, F., *Properties of Electrodeposits. Their Measurement and Significance*. The Electrochemical Society, New Jersey, 1975.
- [36] Glasstone, S., *The Fundamentals of Electrochemistry and Electrodeposition*. Franklin Publishing Company, New Jersey, 1943.
- [37] Heng, K.-h., *Development of an AC Type Micropump Based on Magnetohydrodynamic (MHD) Principle* in The Department of Mechanical Engineering, Louisiana State University, Baton Rouge, 2001.
- [38] Lorenz, H., et al., *SU-8: A Low Cost Negative Resist for MEMS*. J. Micromech., 1997. 7, pp. 121-124.
- [39] Lorenz, H., et al., *High-aspect-ratio, Ultrathick, Negative-tone Near-UV Photoresist and Its Applications for MEMS*. Sensors and Actuators, 1998. A64, pp. 33-39.

- [40] Morris, T., *Fabrication and Assembly of an Array of Micro Fuel Injector Nozzles for a Trapped Vortex Combustor* in The Department of Mechanical Engineering, Louisiana State University, Baton Rouge, 2002.
- [41] Dann-Johnson, S., *Materials Characterization of UV-LIGA Fabricated Fatigue Specimens* in The Department of Mechanical Engineering, Louisiana State University, Baton Rouge, 2001.
- [42] Ling, Z., Lian, K., and Jian, L. *Improved Patterning Quality of SU-8 Microstructures by Optimizing the Exposure Parameters* in *The International Society for Optical Engineering: Advances in Resist Technology and Processing XVII Proc.* Santa Clara, California: 27 February - 3 March, 2000. pp. 1019-1027.
- [43] Roark, R.J. and W.C. Young, *Formulas for Stress and Strain*. Sixth ed. 1989, New York: McGraw Hill.

VITA

Miss Oropeza was born on February 16th, 1975, in Mérida, Venezuela. She received the degree of Bachelor in Science in Engineering from The Mechanical Engineering and Materials Science Department at Duke University located in Durham, North Carolina, in May of 1997. She was employed at Baker Oil Tools in Venezuela from August 1997 to July 1999. Since joining the graduate program at Louisiana State University (LSU) in August of 1999, she has been a member of the Microsystems Engineering Team (μ set). Currently she is a candidate for the degree of Master in Science in Mechanical Engineering, to be awarded during the LSU commencement ceremonies in the Spring of 2002. She will begin her employment with the Shell International Exploration and Production Technology and Research group in Houston, Texas, as a Production Engineer, in May 2002.